The Astrophysical Journal Supplement Series, 239:33 (17pp), 2018 December https://doi.org/10.3847/1538-4365/aaed3b

Determining the Core Radio Luminosity Function of Radio AGNs via Copula

Zunli Yuan[1,2,3], Jiancheng Wang[1,2,3], D. M. Worrall[4], Bin-Bin Zhang[5,6], and Jirong Mao[1,2,3]
[1] Yunnan Observatories, Chinese Academy of Sciences, Kunming 650216, People's Republic of China; yuanzunli@ynao.ac.cn
[2] Key Laboratory for the Structure and Evolution of Celestial Objects, Chinese Academy of Sciences, Kunming 650216, People's Republic of China
[3] Center for Astronomical Mega-Science, Chinese Academy of Sciences, Beijing 100012, People's Republic of China
[4] HH Wills Physics Laboratory, University of Bristol, Tyndall Avenue, Bristol BS8 1TL, UK
[5] School of Astronomy and Space Science, Nanjing University, Nanjing 210093, People's Republic of China
[6] Key Laboratory of Modern Astronomy and Astrophysics (Nanjing University), Ministry of Education, People's Republic of China
Received 2018 September 9; revised 2018 October 21; accepted 2018 October 27; published 2018 December 18

Abstract

The radio luminosity functions (RLFs) of active galactic nuclei (AGNs) are traditionally measured based on total emission, which does not reflect the current activity of the central black hole. The increasing interest in compact radio cores of AGNs motivates determination of the RLF based on core emission (i.e., core RLF). In this work we have established a large sample (totaling 1207) of radio-loud AGNs, mainly consisting of radio galaxies (RGs) and steep-spectrum radio quasars (SSRQs). Based on the sample, we explore the relationship between core luminosity (L_c) and total luminosity (L_t) via a powerful statistical tool called "Copula." The conditional probability distribution $p(\log L_c|\log L_t)$ is obtained. We derive the core RLF as a convolution of $p(\log L_c|\log L_t)$ with the total RLF that was determined by previous work. We relate the separate RG and SSRQ core RLFs via a relativistic beaming model and find that SSRQs have an average Lorentz factor of $\gamma = 9.84^{+3.61}_{-2.50}$, and that most are seen within $8^\circ \lesssim \theta \lesssim 45^\circ$ of the jet axis. Compared with the total RLF, which is mainly contributed by extended emission, the core RLF shows a very weak luminosity-dependent evolution, with the number density peaking around $z \sim 0.8$ for all luminosities. Differences between core and total RLFs can be explained in a framework involving a combination of density and luminosity evolutions where the cores have significantly weaker luminosity evolution than the extended emission.

Key words: galaxies: active – galaxies: luminosity function, mass function – radio continuum: galaxies

Supporting material: machine-readable table

1. Introduction

Observations have suggested that radio-loud active galactic nuclei (AGNs) play an important role in feedback, and thus have a significant impact on galaxy evolution (e.g., Bower et al. 2006; Croton et al. 2006; Fabian 2012; McAlpine et al. 2013). This type of AGN, which at high powers includes radio galaxies (RGs) and quasars, displays double lobes connected to a "core" by jets on scales of ~100 kpc. In unification schemes, quasars are the beamed end-on counterparts of RGs. An RG can be generically described by a three-component structure of core, jets, and lobes. The core, which is traditionally defined as a component unresolved on arcsecond scales and with a flat radio spectrum (e.g., Hardcastle et al. 1998; Mullin et al. 2008), is one of the most important structures in radio-loud AGNs, as it marks where the active nucleus propels energy and matter to extended lobes via jets. The standard interpretation that the core is the optically thick base of the jet (e.g., Blandford & Königl 1979), has been confirmed by VLBI maps (e.g., Antonucci 2011).

The radio core emission is generally thought to be self-absorbed nonthermal synchrotron emission originating in the inner jet (e.g., Verdoes Kleijn et al. 2002; Kharb & Shastri 2004; Kim et al. 2018). It is directly associated with processes in the central engine, and related to accretion and triggering of the supermassive black hole (SMBH). At low radio frequencies, the core is often only about 0.001 times the flux density of the total source. The core and jets are affected by relativistic beaming that causes orientation dependencies. The lobes, which display extended structures and are composed of old plasma, dominate the low-frequency emission of the source and are not affected by relativistic effects, but do not relate directly to current processes in the central engine.

The radio luminosity function (RLF) is an important statistical tool used to study the evolution of radio sources. Up to now most research on the RLFs of radio-loud AGNs has been based on their total radio emission (i.e., total RLF, e.g., Dunlop & Peacock 1990; Willott et al. 2001; McAlpine & Jarvis 2011; Yuan et al. 2016). In principle, we can also determine RLFs based on core emission (i.e., core RLFs), and can expect that the core RLF would be more closely associated with the fundamental physical processes creating and maintaining jets than the total RLF, which is strongly affected by time-averaged properties and the environment.

The motivation of this work is based on the importance of the core RLF. It can be important in the following ways. First, the shape and evolution of the core RLF provide more rigorous constraints on the nature of the instantaneous radio activity in massive galaxies. Since core radio activity arises within a very small (<1 pc) region (e.g., Sadler et al. 1995), the difference between radio-loud and radio-weak AGNs is established already on the parsec scale (Falcke & Biermann 1995). Second, the core RLF helps us to understand the accretion process onto SMBHs more directly than that for the total RLF: the core's radiation is closely linked with the properties of the SMBH, while environmental effects play an important role for the large-scale lobes. For example, the observed relation between BH mass and radio and X-ray luminosity (known as the fundamental plane of active BHs) that defines the physical state of low kinetic mode objects (see Merloni & Heinz 2008) is based on the observed (5 GHz) radio core emission (e.g.,

Hardcastle et al. 2009), not on the extended one. Third, galaxies have weak radio emission on extended scales that is unrelated to the AGN-related emission (i.e., starburst related instead), and total RLFs run into the problem that they start picking up such objects at low luminosities and so are no longer measuring AGN characteristics. That is less of a problem for a core RLF. Fourth, the increasing interest in compact radio cores with the forthcoming advent of the Square Kilometre Array (SKA) requires determination of the core RLF. The presence of a compact radio core in the nuclei of galaxies is usually believed to be a clear sign of BH activity (e.g., Baldi et al. 2018). In view of this, Falcke et al. (2004) argued that the radio emission from compact cores can be used effectively for large radio surveys with the SKA, and these cores can be used to study the evolution of BHs throughout the universe and even to detect the very first generation of BHs.

Interest in the cores of RGs is reflected in studies at radio frequencies $\gtrsim$10 GHz (e.g., Whittam et al. 2013; Sadler et al. 2014; Whittam et al. 2015) based on, for example, the Tenth Cambridge (10 C) Survey (AMI Consortium et al. 2011) and the Australia Telescope 20 GHz (AT20G) survey (Murphy et al. 2010). For high-frequency selected sources, the radio emission arises mainly from the core (e.g., Sadler et al. 2006), and many sources lack extended radio emission and are analogous to FR 0s (e.g., Baldi et al. 2015). These recent studies have suggested that the radio core is a key component to understanding the faint source population at high-frequency (also see Whittam et al. 2017).

Up to now, observed data on core flux densities have been abundant, but establishing a complete core sample with good control over the selection function is still rather difficult. On one hand, at low frequencies radio surveys of AGN are selected based on total emission but not on core emission. Obviously, completeness in total flux is not the same thing as completeness in core flux. On the other hand, at high frequencies, a flat-spectrum core is dominant, so flux-limited complete samples at high frequencies are biased toward quasars and sources with bright beamed core emission. Therefore, the relativistic beaming effect creates further challenges for the estimation of the core RLF. Due to the above factors, a comprehensive and reliable description of the core RLF is still absent.

To estimate the core RLF, some more sophisticated statistical approach should be adopted, in which the problem of sample completeness, as well as the relativistic beaming of core emission, are taken into account. In regard to beaming, our plan is to use a steep-radio-spectrum source sample only, which will be discussed in Section 2. On the issue of the sample completeness problem, coincidentally, the difficulty in estimating the core RLF is very similar to that of determining the black hole mass functions (BHMFs). The BHMF is derived by applying the existing relations between $M_{\rm BH}$ and host galaxy properties to galaxy luminosity or velocity functions (e.g., Marconi et al. 2004). Similarly, we can derive the core RLF by applying a relation between core and total radio luminosities to the total RLF, which is well determined. To give a mathematically rigorous description of the core–total relation, we resort to a special statistical tool called "Copula," which is developed by modern statistics to describe the dependence between random variables. In recent years, copula has been widely used in various areas such as finance and hydrology, but its application in astronomy or astrophysics is limited (Benabed et al. 2009; Jiang et al. 2009; Koen 2009; Scherrer et al. 2010; Takeuchi 2010; Koen & Bere 2017).

The paper is organized as follows. Section 2 describes the properties of the sample. In Section 3, the core to total radio luminosity correlation is analyzed. Section 4 introduces the concept of copula, and presents the correlation described by copula.[7] The core RLF is derived in Section 5. Section 6 discuss the difference between core and total RLFs. The main results of the work are summarized in Section 7. Throughout the paper, we adopt a lambda cold dark matter cosmology with the parameters $\Omega_m = 0.27$, $\Omega_\Lambda = 0.73$, and $H_0 = 71\ {\rm km\ s^{-1}\ Mpc^{-1}}$.

2. The Sample

Radio-loud quasars are traditionally classified into two main categories: steep spectrum (SSRQs $\alpha > 0.5$, assuming $S_\nu \propto \nu^{-\alpha}$) and flat spectrum (FSRQs, $\alpha < 0.5$). According to unification schemes (e.g., Antonucci 1993; Urry & Padovani 1995), the appearance of the steep/flat-spectrum dichotomy depends primarily on axis orientation relative to the observer, while intrinsic properties are similar. Steep-spectrum sources include RGs and SSRQs, and are lobe-dominated and inclined at larger angles to the line of sight compared with their flat-spectrum counterparts. Due to the relatively larger viewing angles, the radio cores in steep-spectrum sources are much less affected by Doppler-boosting compared with those in flat-spectrum sources. Therefore, we will use a steep-spectrum source sample only to determine the core RLF. This choice will lead to missing many cores of flat-spectrum sources, but the bias can be quantified as long as the unification scheme of AGNs is true and the inclination angles of radio sources are randomly distributed. The core RLF derived from the steep-spectrum sources would then be different from the intrinsic core RLF only in normalization factor, but not in shape (e.g., Liu & Zhang 2007).

2.1. The Sample Composition

This work involves two samples, referred to as Samples I and II. Sample I is a complete "coherent" (e.g., Avni & Bahcall 1980) sample consisting of four subsamples with different flux limits. It was established by our previous work (Yuan & Wang 2012), and was used to determine the total RLF by Yuan et al. (2017, hereafter Y17). Y17's total RLF is the important base for this work. Sample II is the base to explore the relationship between core and total luminosities via copula. It inherits all the sources (totaling 631) that have both total and core flux density measurements from Sample I. It also absorbs the 73 sources from the GRG (giant RG) sample by Lara et al. (2004). Through an extensive literature search we collect 503 additional sources and put them into Sample II. A list of these 503 sources can be found in Appendix A. Sample II thus includes 1207 radio-loud AGNs that mainly consist of RGs and SSRQs. In statistics, a simple random sample is a subset of individuals (a sample) chosen from a larger set (a population). Each individual is chosen randomly and entirely by chance (Yates et al. 2008). The data of Sample II are collected from various sources. It can be treated approximately as a simple random sample.

2.2. Sample II

All the sources in Sample II have radio core flux densities at 5 GHz, total radio flux densities at 408 MHz or 1.4 GHz, and

[7] A computer routine for performing the copula analysis in this work is available upon request from Z. Yuan. A general-purpose copula analysis code will be made available on https://github.com/yuanzunli.

Table 1
Completeness of the Data

Ident.	z	$S_{c5.0}$	$S_{t0.408}$	$S_{t1.4}$	α_t	α_c	Total
RGs	752	752	682	70	682	388	752
quasars	455	455	452	3	452	232	455

redshifts. The source composition, and the numbers of sources for which parameters of interest are measured, are shown in Table 1. In the table, $S_{c5.0}$ represents the radio core flux density at 5 GHz and z is redshift. $S_{t0.408}$ and $S_{t1.4}$ represent the total radio flux densities at 408 MHz and 1.4 GHz, respectively. α_t is the spectral index near 408 MHz for total emission, and α_c represents the core spectral index near 5 GHz. Note that the 73 sources from Lara et al. (2004) only have total radio flux densities measured at 1.4 GHz. We will apply spectral indices to them using a Monte Carlo method (see Section 3.3 for detail), and then convert S_{t1400} to S_{t408} so that for all the sources, a monochromatic luminosity at 5 GHz for cores, and 408 MHz for total emission, can be calculated. Throughout the paper, when it comes to the core and total luminosities (denoted as L_c and L_t respectively), we always mean the 5 GHz and 408 MHz monochromatic luminosities, respectively.

3. Data Analysis

3.1. Mathematical Notation

We use an italic capital letter to denote a random variable; e.g., L_c is the core luminosity or its value, while L_C denotes the random variable. We use the common statistical notation that an estimate of a quantity is denoted by placing a "hat" above it; e.g., $\hat{\theta}$ is an estimate of the true value of the parameter θ. We use a non-parametric method, called kernel density estimation (KDE), to estimate the probability density function (PDF) of a random variable. Let $(x_1, x_2, \cdots, x_n)$ be a univariate independent sample drawn from some distribution with an unknown density $f(x)$. The KDE of this function f is given by

$$f(x) \cong \hat{f}_h(x) = \frac{1}{nh}\sum_{i=1}^{n} K\left(\frac{x - x_i}{h}\right), \quad (1)$$

where K is the kernel (a non-negative function that integrates to one), and $h > 0$ is a smoothing parameter called the bandwidth. The normal kernel is often used, which means taking $K(x)$ as the standard normal density function. The bandwidth of the kernel is a free parameter that exhibits a strong influence on the resulting estimate. We follow the method of Botev et al. (2010) to chose an optimal h.

3.2. The Spectral Index Distribution

The distributions of spectral indices for radio core and total emission are shown in Figure 1. The black thick solid and black dotted curves represent the core spectral indices of RGs and SSRQs, respectively. These curves are plotted based on the KDE. We note that the two curves have similar means and standard deviations. In Figure 1, the black dashed curve shows the Gaussian fit for the RG+SSRQ core spectral indices. The spectral index distributions of total emission for RGs (cyan thick solid curve) and SSRQs (blue dashed curve) are even more similar. The red dashed curve shows the Gaussian fit for the RG+SSRQ total spectral indices. The mean and standard deviation of Gaussian fits for the core and total spectral indices are given in Table 2.

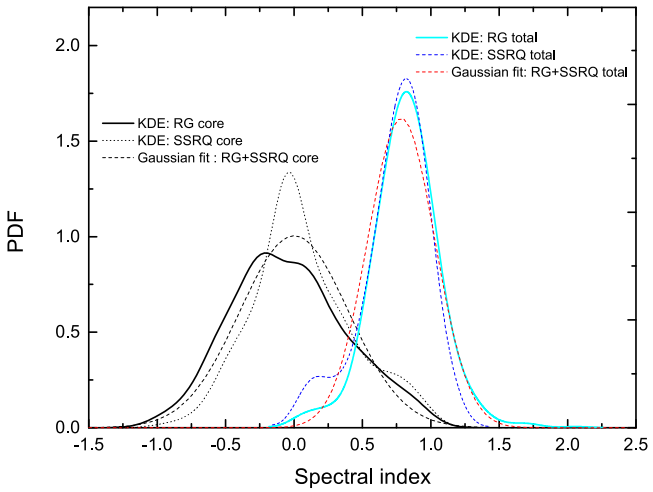

Figure 1. Distributions of the core and total spectral indices; the meaning of each curve is explained in Section 3.2.

Table 2
Gaussian Fits to the Spectral Index Distribution

	RG+SSRQ Core	RG+SSRQ Total
Mean	0.001	0.785
Sigma	0.397	0.246

3.3. Dealing with the Spectral Index Incompleteness

In our RG sample, 9.3% of the sources do not have a total spectral index, and 48.3% of the sources do not have a core spectral index. For the SSRQ sample, the two percentages are 0.66% and 49%, respectively. For the sources without spectral indices, we assume the spectral indices follow Gaussian distributions (with means and sigmas given in Table 4), and assign random spectral indices to them with a Monte Carlo method. We create 10,000 simulated samples of the 752 RGs and 455 SSRQs, in which the sources with *total* spectral indexes less than 0.4 (e.g., Chhetri et al. 2012) are excluded from the analysis. The minimum spectral index criterion means statistically that all the sources entering the analysis are lobe-dominated. In the following sections, we will introduce the analysis process, which is done independently for each simulation. The final result is built as the average of the results, and its uncertainty takes into account the spread of all the Monte Carlo results (also see Ajello et al. 2014).

3.4. The Core–Total Radio Luminosity Correlation

Note that there is a correlation between the core and total radio luminosities in radio AGNs (e.g., Giovannini et al. 1988; Zirbel & Baum 1995; Lara et al. 2004; Liu & Zhang 2002). In Figure 2, the core luminosity versus the total luminosity for our sample is plotted, with the RGs and SSRQs being shown as black squares and red stars, respectively. Statistically, the core and total radio luminosities can be regarded as random variables L_C and L_T. The $L_c - L_t$ correlation means that a dependence exists between L_C and L_T. However, caution must be taken when treating the $L_c - L_t$ correlation, because both L_C and L_T may strongly correlate with redshift and this could result

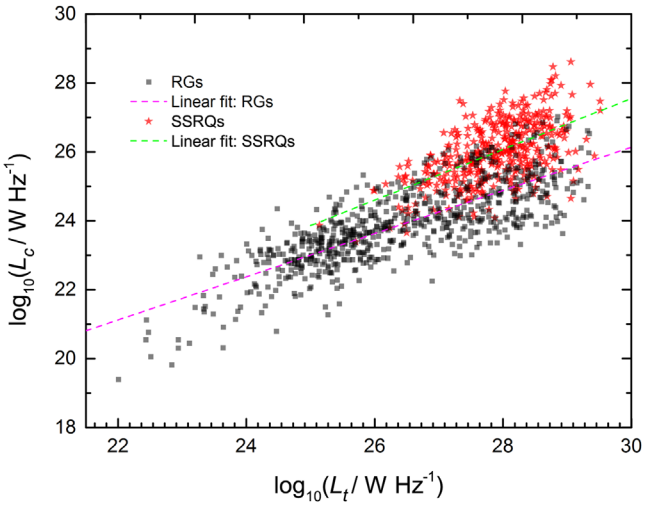

Figure 2. Correlation of core luminosity at 5 GHz vs. total luminosity at 408 MHz. The black squares and red stars represent RGs and SSRQs, respectively. The magenta and green dashed lines show the linear fits, i.e., $\log L_c = \log L_t \times (0.63 \pm 0.02) + (7.34 \pm 0.48)$ for RGs, and $\log L_c = \log L_t \times (0.74 \pm 0.05) + (5.42 \pm 1.47)$ for SSRQs.

in a spurious luminosity correlation (e.g., Padovani 1992). The proper way of dealing with the problem is to examine the $L_c - L_t$ correlation and eliminate the effect of redshift, i.e., via a partial correlation analysis (e.g., Ghirlanda et al. 2011; Inoue 2011, see Appendix B for details). This is performed for our Monte Carlo simulated samples. We calculate that the average partial correlation coefficients and p-values are 0.289 and 1.002×10^{-14} for RGs, and 0.232 and 3.910×10^{-6} for SSRQs, respectively. Thus, the partial correlation analysis suggests that the $L_c - L_t$ correlation is genuine.

Traditionally, the $L_C - L_T$ dependence was assumed to be linear in logarithmic space. For example, Zirbel & Baum (1995) found $\log L_c = \log L_t \times (0.56 \pm 0.04) + (9.0 \pm 1.0)$ for RGs. Based on high-quality data of the core flux density observed with VLBI, Giovannini et al. (2001) found $\log L_c = \log L_t \times (0.62 \pm 0.04) + (7.6 \pm 1.1)$ for their RG sample. These are very similar to our result that the linear fit is $\log L_c = \log L_t \times (0.63 \pm 0.02) + (7.34 \pm 0.48)$ for RGs (the magenta dashed line in Figure 2). However, from the perspective of statistics, the linear correlation does not rest on a strong mathematical foundation. In the modern field of statistics, scientists have developed a special statistical tool called "Copula" to describe the dependence between random variables. Besides the linear dependence, we can capture the nonlinear, asymmetric and tail dependence between variables by copula functions.

4. Copula

4.1. A Brief Introduction

Briefly speaking, copulas are functions that join or "couple" multivariate distribution functions to their one-dimensional marginal distribution functions (Nelson 2006). According to Sklar's theorem, let H be a joint distribution function with marginal distribution functions F and G; if F and G are continuous, then there exists a unique copula C such that

$$H(x, y) = C(F(x), G(y)). \tag{2}$$

Let $u_n = F(x_n)$ and $v_n = G(y_n)$, $n = 1, 2, \ldots N$. u_n and v_n obey the uniform distribution on [0, 1]. Hence, a copula $C(u, v)$ can be regarded as the joint distribution of random vectors (U,V) whose one-dimensional margins are uniform distributions on [0, 1] (Nelson 1999). Concerning rigorous definition and detailed introduction of copula, we refer the interested reader to Nelson (2006).

As a joint distribution function, H not only carries the information on the marginal distribution of each variable, but also implies the dependence properties between variables. The main appeal of Equation (2) is that by using copulas one can model the dependence structure and the marginal distributions separately. All the information on the dependence between variables is carried by the copula. From Equation (2), the joint probability density function $h(x, y)$ can be written as

$$h(x, y) = c(F(x), G(y))f(x)g(y), \tag{3}$$

where $f(x)$ and $g(y)$ are the marginal PDFs, and $c(u, v)$ is given by

$$c(u, v) = \frac{\partial^2 C(u, v)}{\partial u \partial v}. \tag{4}$$

The conditional probability density function of Y given the occurrence of the value x of X can be written as

$$f_Y(y|X = x) \equiv \frac{h(x, y)}{f(x)} = c(F(x), G(y))g(y). \tag{5}$$

Copulas consists of many families, of which the elliptical and Archimedean Copulas are most common. For example, the normal copula is an elliptical copula given by

$$C_\rho(u, v) = \int_{-\infty}^{\Phi^{-1}(u)} \int_{-\infty}^{\Phi^{-1}(v)} \frac{1}{2\pi\sqrt{1-\rho^2}} \exp\left[-\frac{s^2 - 2\rho st + t^2}{2(1-\rho^2)}\right] dsdt, \tag{6}$$

where Φ^{-1} is the inverse of the standard normal distribution function and ρ, the linear correlation coefficient, is the copula parameter.

4.2. Copula Modeling

The purpose of copula modeling is to find an optimal copula function and also estimate its parameters to describe the observed data (X_i, Y_i). In this work, we use the maximum likelihood estimate (MLE) method to estimate the parameters of a copula function. For some target copula with the parameter θ, the likelihood function of the sample (X_i, Y_i), $(i = 1, 2, \ldots, n)$ is given by

$$L(\theta) = \prod_{i=1}^{n} c[F(x_i), G(y_i), \theta] f(x_i) g(y_i). \tag{7}$$

According to the MLE, the estimate of θ is $\hat{\theta} = \arg\max \ln L(\theta)$. Once the parameters θ of a group of target copula functions are estimated, we will use the Akaike information criterion (AIC, Akaike 1974) to select an optimal copula (e.g., Sato et al. 2011). The AIC is given by

$$\mathrm{AIC} = -2\sum_{i=1}^{n} \ln c[F(x_i), G(y_i), \theta] + 2p_k, \tag{8}$$

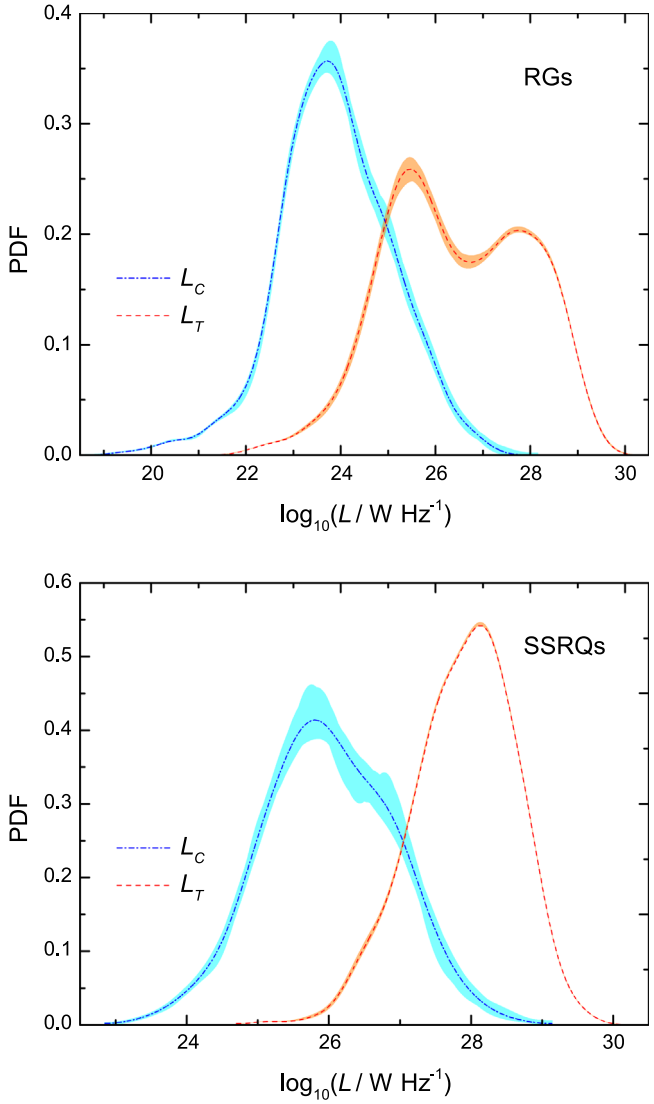

Figure 3. Distribution of L_C and L_T for RGs and SSRQS. The light shaded areas, estimated by 10,000 Monte Carlo simulations, represent the uncertainties due to the incompleteness of spectral indices. The dashed–dotted and dashed curves represent the average of the Monte Carlo results.

where p_k is the number of free parameters in the copula model. We will take the copula with the smallest AIC value as the optimal copula.

4.3. Marginal PDFs

In Equation (7), the marginal PDFs $f(x)$ and $g(y)$ need to be estimated. This can be easily realized using non-parametric estimation (e.g., KDE) or a parametric method such as MLE. Once $f(x)$ is known, $F(x)$ is simply given by

$$F(x) = \int_{-\infty}^{x} f(x)dx, \tag{9}$$

similarly, for $G(y)$ and $g(y)$.

Take our RG sample, for example: the KDE estimated marginal PDFs of L_T and L_C are given in Figure 3. The red and blue dashed curves show the KDE result from the average of the Monte Carlo simulations. The shaded orange and cyan bands represent the uncertainty, taking into account the spread of all the Monte Carlo simulation results. The reason for the bimodal shape of the PDF(L_t) for RGs is presumably due to a deficit of FRI/II boundary sources in our RG sample. It is well known that the FRI and II morphological classifications (Fanaroff & Riley 1974) strongly correlate with radio power: radio sources with $L_{408\ \mathrm{MHz}} \lesssim 10^{25}\ \mathrm{W\ Hz^{-1}}$ are dominated by FR Is, while those with $L_{408\ \mathrm{MHz}} \gtrsim 10^{27}\ \mathrm{W\ Hz^{-1}}$ are almost exclusively FR IIs (Zirbel & Baum 1995). The unimodal shape of PDF(L_c) for RGs indicates that the difference between the radio core powers of FR Is and FR IIs is less than the difference between the extended radio powers, consistent with the study by Zirbel & Baum (1995).

Note that for both RGs and SSRQs, the KDE estimated PDF(L_c) is still not smoothed enough to take as an ideal approximation of the true PDF, and this will affect the smoothness of the final core RLF. We then use a parametric method to estimate the marginal PDF $g(\log L_c)$, i.e., model it as a normal distribution

$$g(\log L_c) = \frac{1}{\sqrt{2\pi\sigma^2}} e^{-\frac{(\log Lc-\mu)^2}{2\sigma^2}}, \tag{10}$$

where μ and σ are free parameters to be estimated by MLE.

4.4. Copulas for $Lc - L_t$

We have examined 31 published copulas and applied the procedure introduced in Section 4.2 to our simulated samples to find the best two for our data. The first one is the normal copula given by Equation (6). The second one is the number 13 Archimedean copula from Nelson (2006, hereafter N13 copula) formulated as

$$C_\theta(u, v) = e^{1-[(1-\ln u)^\theta + (1-\ln v)^\theta - 1]^{\frac{1}{\theta}}}, \tag{11}$$

where θ is the parameter, and $\theta \in (0, \infty)$.

In Figure 4, we show the distributions of the best-fit parameters of the N13 and normal copula models for our Monte Carlo samples, as well as the distributions of AIC values for the two copula modelings. The upper and lower panels correspond to RGs and SSRQs, respectively. Table 3 summarizes the means of best-fit parameters and AIC values for the Monte Carlo samples. For both the RG and SSRQ samples, the N13 copula model has lower AIC values, and we will take it as the optimal copula.

4.5. Tail Dependence

Tail dependence is an important concept in copula theory. Let X and Y be continuous random variables with distribution functions F and G, respectively. The upper/lower tail dependence parameter λ_U/λ_L is the limit (if it exists) of the conditional probability that Y reaches extremely large/small values given that X attains extremely large/small values (Nelson 2006), i.e.,

$$\lambda_U = \lim_{t\to 1^-} P[Y > G^{-1}(t) | X > F^{-1}(t)], \tag{12}$$

and

$$\lambda_L = \lim_{t\to 0^+} P[Y \leqslant G^{-1}(t) | X \leqslant F^{-1}(t)]. \tag{13}$$

From the above equations, we calculate that for both the normal and N13 copulas, $\lambda_U = \lambda_L = 0$. This implies that L_T and L_C are tail-independent, meaning that when the cores reach extreme luminosities the probability that lobes also show extreme luminosities tends to zero. Physically, this can be understood as

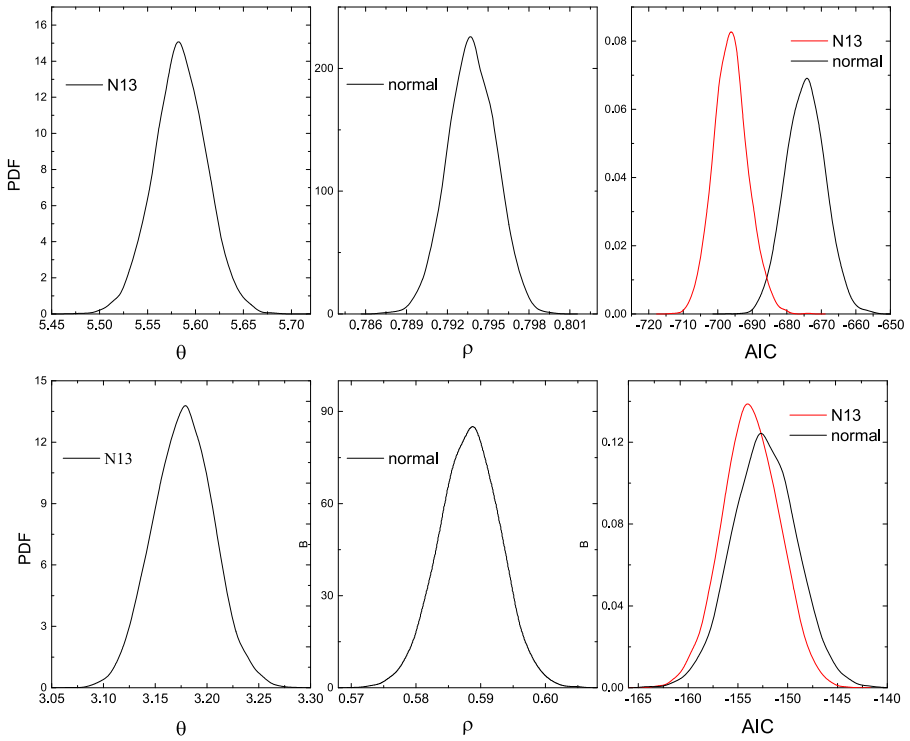

Figure 4. Left and middle panels: distributions of the best-fit parameters of the N13 and normal copula models for our Monte Carlo simulated samples. Right: distributions of the AIC values for the N13 (red curve) and normal (black curve) copula modelings. The upper and lower panels are for RGs and SSRQs, respectively.

Table 3
Means of the Best-fit Copula Parameters and AIC Values

	$\hat{\theta}$	$\hat{\rho}$	AIC N13	AIC Normal
RGs	5.584	0.794	−696.17	−674.55
SSRQs	3.178	0.588	−153.73	−152.35

follows. The core and total (mainly contributed by extended emission) luminosities are correlated because the core and extended emission relate to the same jet kinetic power. Nevertheless, these two measurements have different timescales: extended radio luminosity is a proxy for time-averaged jet power on timescales of tens to hundreds of Myr, while core luminosity traces the instantaneous jet power (see Shabala 2018). In addition, the lobe emission is more affected by external environment (e.g., Falcke et al. 2004), such as the density of intergalactic medium (IGM). Both the timescale and environment factors weaken the connection between core and extended radio luminosities. When one of them reaches extremely large/small values, the other does not respond in time. Examples can be found in recurrent AGNs, as evidence is growing that AGN activity could be episodic (e.g., Saikia & Jamrozy 2009; Brocksopp et al. 2011; Liao et al. 2016). During the phase of inactivity, sources may lack certain features, such as radio cores or well-defined jets that are produced by continuing activity, while the radio lobes still undergo a period of fading before they disappear completely (Marecki & Szablewski 2009). During the phase of reactivation, very faint fossil radio lobes remaining from an earlier active epoch can be observed, along with newly restarting jets and cores (Murgia et al. 2011). In these two situations, we can observe extremely low-luminosity cores or lobes.

5. Determining the Core RLF

The RLF is defined as the number of sources per comoving volume with luminosities in the range $\log L$, $\log L + d\log L$

$$\rho(z, L) = \frac{d^2N}{dV\, d\log L}. \tag{14}$$

We denote the total RLF as $\rho_t(z, L_t)$, and the core RLF as $\rho_c(z, L_c)$. In a previous work (Y17), we determined the total RLF based on a mixture evolution scenario that takes into account both density evolution (DE) and luminosity evolution (LE). Here, we adopt the Model A of Y17 as the total RLF:

$$\rho_t(z, L_t) = e_1(z)\phi_1\left(\frac{L_t/e_2(z)}{L_*}\right)^{-\beta}\exp\left[-\left(\frac{L_t/e_2(z)}{L_*}\right)^{\gamma}\right], \tag{15}$$

where

$$e_1(z) = \frac{(1+z_c)^{p_1} + (1+z_c)^{p_2}}{\left(\frac{1+z_c}{1+z}\right)^{p_1} + \left(\frac{1+z_c}{1+z}\right)^{p_2}}, \tag{16}$$

and

$$e_2(z) = (1+z)^{k_1}. \tag{17}$$

The parameters and their 1σ error for ρ_t are given in Table 4.

5.1. Semi-parametric Core RLF

Considering the existence of the $L_C - L_T$ correlation, the core RLF can be derived from the total RLF. The process is similar to that used to derive the BHMF (Marconi et al. 2004). The difference is that their correlation description was resorted

Table 4
Input Parameters for ρ_t and Best-fit Parameters for ρ_c

	$\log_{10}\phi_1$	$\log_{10}L_*$	β	γ	z_c	p_1	p_2	k_1
Total RLF	$-4.85^{+0.13}_{-0.12}$	$24.68^{+0.16}_{-0.17}$	$0.44^{+0.02}_{-0.02}$	$0.31^{+0.01}_{-0.01}$	$0.86^{+0.10}_{-0.09}$	$0.31^{+0.22}_{-0.26}$	$-5.92^{+0.18}_{-0.39}$	$4.73^{+0.16}_{-0.09}$
Core RLF RG	$-3.749^{+0.019}_{-0.008}$	$21.592^{+0.015}_{-0.026}$	$0.139^{+0.004}_{-0.007}$	$0.878^{+0.002}_{-0.002}$	$0.893^{+0.017}_{-0.017}$	$2.085^{+0.051}_{-0.077}$	$-4.602^{+0.066}_{-0.057}$	$1.744^{+0.060}_{-0.050}$
Core RLF SSRQ	$-5.066^{+0.047}_{-0.033}$	$24.624^{+0.051}_{-0.073}$	$0.346^{+0.005}_{-0.007}$	$0.976^{+0.008}_{-0.009}$	$0.875^{+0.035}_{-0.021}$	$2.090^{+0.093}_{-0.119}$	$-4.361^{+0.057}_{-0.106}$	$1.413^{+0.088}_{-0.066}$

Note. Units—ϕ_1: (Mpc^{-3}), L_*: ($\mathrm{W\ Hz}^{-1}$).

to the linear relation with a intrinsic dispersion while we use copulas. Consulting Equation (5) and utilizing Equations (1), (4), (9), (10), and (11), the conditional PDF of L_C given $L_T = L_t$ can be calculated as

$$p(\log L_c|\log L_t) = c[F(\log L_t), G(\log L_t)]g(\log L_c). \quad (18)$$

We then define $\rho_t(z, L_t)d\log L_t$ as the number of sources per unit comoving volume at the redshift z, in the luminosity range of $\log L_t$, $\log L_t + d\log L_t$. $p(\log L_c|\log L_t)d\log L_c$ is the probability that L_c is in the range of $\log L_c$, $\log L_c + d\log L_c$ for a given $\log L_t$. Thus, the number of sources with L_c, L_t in the ranges of $\log L_c$, $\log L_c + d\log L_c$ and $\log L_t$, $\log L_t + d\log L_t$ at a redshift of z is

$$\rho(z, L_c, L_t)d\log L_c d\log L_t = p(\log L_c|\log L_t)d\log L_c \times \rho_t(z, L_t)d\log L_t. \quad (19)$$

Finally, the core RLF $\rho_c(z, L_c)$ is the convolution of $\rho_t(z, L_t)$ and $p(\log L_c|\log L_t)$:

$$\rho_c(z, L_c) = \int p(\log L_c|\log L_t)\rho_t(z, L_t)d\log L_t. \quad (20)$$

where the limits of integration are $\log L_{t,\min} = 19$ and $\log L_{t,\max} = 30$, roughly corresponding to the L_t range for the RG sample.

By measuring the $L_C - L_T$ correlations and corresponding copulas for the RG and SSRQ core samples separately, the core RLFs for the two populations are derived by Equation (20). Figure 5 shows the core RLFs at $z = 0.1$, 0.5, 1.0, 2.0, and 3.0 (black, green, and red solid lines; blue and red dashed lines, respectively). The gray bands, estimated by 10,000 Monte Carlo simulations, represent the uncertainties due to the incompleteness of spectral indices. Inspection of Figure 5 suggests that the shape and evolution of the core RLFs for RGs and SSRQs are very similar. The main difference is that SSRQs have higher characteristic luminosity. This is not surprising and can be explained due to beaming. In Figure 6, we show the core RLF of RGs changing with redshift at various luminosities. The black, cyan, red, blue, and green dashed lines show the core RLFs at $\log_{10}L_{5.0\,\mathrm{GHz}} = 19$, 21, 23, 25, and 27 respectively. The light shaded areas take into account not only the uncertainties due to the incompleteness of spectral indices, but also the 1σ error propagated from the total RLF by Y17.

5.2. Parametric Core RLF

The core RLF given in Equation (20) is a semi-parametric function. It is not like the general luminosity functions (LFs), which are obviously seen in DE or/and LE. We use a mixture evolution model similar to that for ρ_t to describe the core RLF. The only difference is replacing the modified Schechter

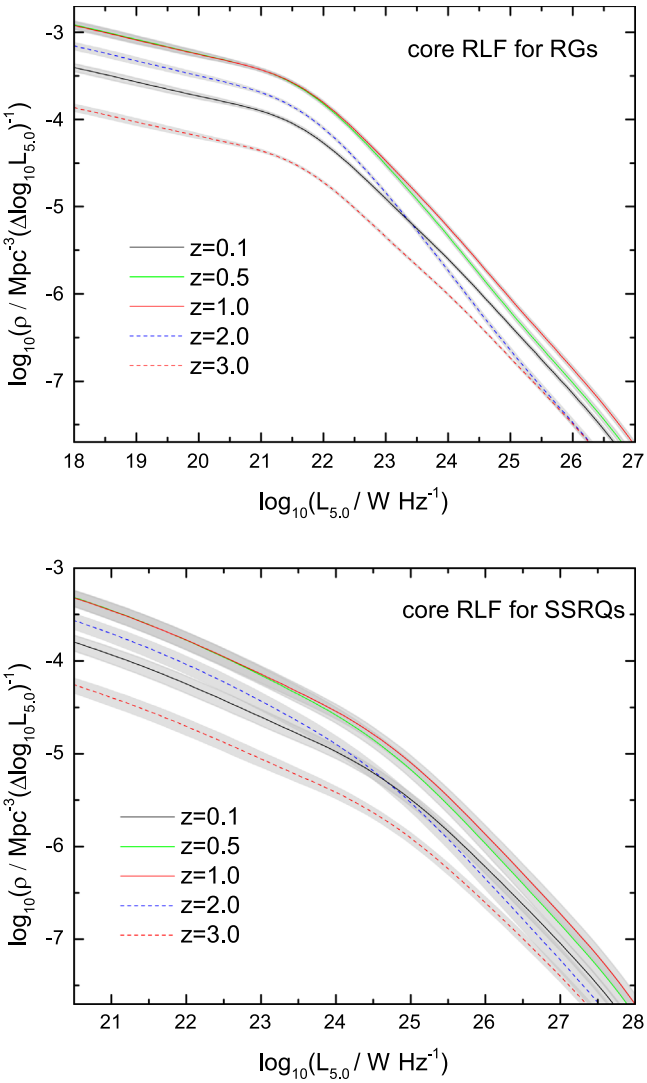

Figure 5. Core RLFs derived by Equation (20) for RGs and SSRQs at $z = 0.1$, 0.5, 1.0, 2.0, and 3.0 (black, green, and red solid lines; blue and red dashed lines, respectively). The gray bands, estimated by 10,000 Monte Carlo simulations, represent the uncertainties due to the incompleteness of spectral indices.

function in Equation (15) with a double power-law form:

$$\rho_c(z, L_c) = e_1(z)\phi_1\left[\left(\frac{L_c/e_2(z)}{L_*}\right)^{\beta} + \left(\frac{L_c/e_2(z)}{L_*}\right)^{\gamma}\right]^{-1}, \quad (21)$$

where $e_1(z)$ and $e_2(z)$ are also given in Equations (16) and (17), respectively. To determine the best-fit parameters in Equation (21), we use a Bayesian Monte Carlo fitting engine

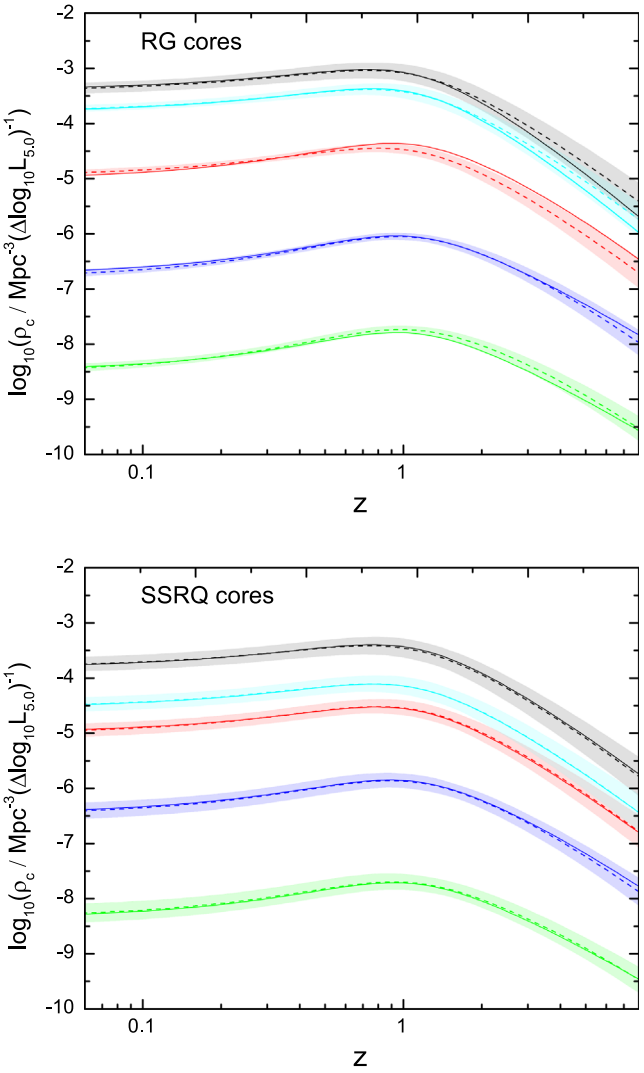

Figure 6. Space densities as a function of redshift for RG and SSRQ cores. For RGs, the black, cyan, red, blue, and green dashed lines show the core RLFs at $\log_{10} L_{5.0\,\mathrm{GHz}} = 19$, 21, 23, 25, and 27, respectively. For SSRQs, these lines represent the core RLF at $\log_{10} L_{5.0\,\mathrm{GHz}} = 21$, 23, 24, 26, and 28, respectively. The light shaded areas take into account the uncertainties due to the incompleteness of spectral indices, as well as the 1σ error propagated from the total RLF by Y17. The solid curves represent the best-fit mixture evolution model of Section 5.2.

(McFit) developed by Zhang et al. (2016). First, we take a group of uniformly spaced points $(z_i, L_i)_{i=1,\ldots,i=N}$ in the $\log L - \log z$ space. For each point, we calculate its $f_{data\,i}$ and $\sigma_{\mathrm{data}\,i}$ by Equation (20), and $f_{\mathrm{mod}\,i}$ by Equation (21). Note that $\sigma_{\mathrm{data}\,i}$ takes into account the uncertainties due to the incompleteness of spectral indices, as well as the 1σ error propagated from the total RLF parameters. Then, the χ^2 is evaluated as

$$\chi^2 = \sum_{i=1}^{N} \left(\frac{f_{\mathrm{data}\,i} - f_{\mathrm{mod}\,i}}{\sigma_{\mathrm{data}\,i}} \right)^2, \tag{22}$$

which is related to the likelihood function by $\chi^2 = -2\ln(\mathrm{likelihood})$. Based on the form of χ^2, the McFit engine obtains the best-fit parameters shown in Table 4. The best-fit core RLFs are shown as solid curves in Figure 6. We find that the mixture evolution model fits the core RLFs well.

5.3. Intrinsic Core RLF

Padovani & Urry (1992) estimated that SSRQs have their radio axes within $14^\circ \lesssim \theta \lesssim 40^\circ$, and high-luminosity RGs are in the range $\theta \gtrsim 40^\circ$. Therefore beaming is important for the cores of SSRQs, while it can be neglected for the cores of RGs. Thus, the core RLF of RGs is close to the intrinsic core RLF. Considering that the total RLF ρ_t in Equation (20) is measured based on steep-spectrum radio sources (Y17), we estimate

$$\rho_c^{\mathrm{intrinsic}}(z, L_c) = \kappa \rho_c^{\mathrm{RG}}(z, L_c), \tag{23}$$

where the value of κ should be equal to the ratio of the total number of steep- and flat-spectrum radio sources to the total number of steep-spectrum radio sources in the universe. Assuming that the steep- and flat-spectrum radio sources are divided by the critical viewing angle of 14°, we have $\kappa \approx 1/\cos 14^\circ = 1.0306$. κ is very close to one, suggesting that the RG core RLF can be regarded as the intrinsic one.

The cores of SSRQs are expected to be the Doppler-beamed counterparts of RG cores. In principle, the core RLFs of SSRQs can be derived from the core RLFs of RGs by considering beaming effect. For a RG core with a luminosity of L_c, after beaming it will be observed as a quasar core with a luminosity of $\mathcal{L}_c$,

$$\mathcal{L}_c = L_c \delta^q, \tag{24}$$

with $q = 2 + \alpha$ for a continuous jet and $q = 3 + \alpha$ for a moving, isotropic source (Urry & Padovani 1995). Other values of q are also possible, e.g., Ajello et al. (2012) adopted a value of $q = 4$ that applies to the case of jet emission from a relativistic blob radiating isotropically in the fluid frame. In Equation (24), δ is the kinematic Doppler factor defined as

$$\delta = (\gamma - \sqrt{\gamma^2 - 1}\cos\theta)^{-1}, \tag{25}$$

where $\gamma = 1/\sqrt{1-\beta^2}$ is the Lorentz factor, β is the bulk velocity in units of speed of light, and θ is the inclination angle. To quantify the beaming effort, we need to know the PDF $P_\delta(\delta)$ for δ. Traditionally, the jet angles are assumed to be randomly distributed within $0^\circ \leqslant \theta \leqslant 90^\circ$. Based on this assumption, the $P_\delta(\delta)$ was determined by Lister (2003). Some later researchers (e.g., Liu & Zhang 2007; Cara & Lister 2008; Ajello et al. 2012) followed this determination. However, for a specific population of AGNs (e.g., SSRQs), the jet angles should be (randomly) distributed within $\theta_2 \leqslant \theta \leqslant \theta_1$ but not necessarily $0^\circ \leqslant \theta \leqslant 90^\circ$. Thus, the formula calculating $P_\delta(\delta)$ by Lister (2003) should be modified to apply to more general conditions. Here we give the generalized formula for deriving $P_\delta(\delta)$ (see the Appendix C, Equation (43) for its detailed definition and deduction) as

$$P_\delta(\delta) = \frac{\delta^{-2}}{\cos\theta_2 - \cos\theta_1} \int_{A(\delta)}^{B(\delta)} \frac{P_\gamma(\gamma)}{\sqrt{\gamma^2 - 1}} d\gamma, \tag{26}$$

where $P_\gamma(\gamma)$ is the PDF for γ. Little is known about the form of $P_\gamma(\gamma)$. In previous works (e.g., Lister 2003; Cara & Lister 2008; Ajello et al. 2012), a power-law form with index k was usually assumed:

$$P_\gamma(\gamma) = C\gamma^k, \tag{27}$$

where C is a normalization constant and the function is valid for $\gamma_1 \leqslant \gamma \leqslant \gamma_2$. In this work, we also test a form similar to the relativistic Maxwell-Jüttner distribution (e.g., Kroon & Becker 2016) for $P_\gamma(\gamma)$. In physics, the Maxwell-Jüttner distribution is the distribution of speeds of particles in a hypothetical gas of relativistic particles. We have

$$P_\gamma(\gamma) = \frac{\gamma\sqrt{\gamma^2-1}\exp(-\gamma/k)}{kK_2(1/k)}, \quad (28)$$

where k is a free parameter, and K_2 denotes the modified Bessel function of the second kind. This function is valid for $1.0 < \gamma < \infty$. In practical calculations, we take a range of $1.01 \leqslant \gamma \leqslant 100$, which can ensure a good normalization.

Given the $P_\delta(\delta)$ and utilizing Equation (24), it is easy to determine the conditional probability distribution of $\log \mathcal{L}_c$ given $\log L_c$. In Appendix D, we give the formula of $p(\log \mathcal{L}_c|\log L_c)$ for two cases: q is a constant (Equation (51)), and q follows the Gaussian distribution (Equation (55)). A Monte Carlo simulation suggests that the two cases give similar results. In the following analysis, we adopt the first case for its simplicity, and

$$p(\log \mathcal{L}_c|\log L_c) = \frac{\ln 10}{q}\left(\frac{\mathcal{L}_c}{L_c}\right)^{\frac{1}{q}} P_\delta\left(\left(\frac{\mathcal{L}_c}{L_c}\right)^{\frac{1}{q}}\right). \quad (29)$$

Now, similar to Equation (20), the Doppler-beamed RG core RLF is calculated as

$$\phi_c(z, \mathcal{L}_c) = \int p(\log \mathcal{L}_c|\log L_c)\rho_c(z, L_c)d\log L_c, \quad (30)$$

where the limits of integration are $\log L_{c,\min} = 18$ and $\log L_{c,\max} = 28$, roughly corresponding to the L_c range for the RG sample. By fitting Equation (30) to the SSRQ core RLF, we can determine the parameters of the Lorentz-factor distribution, and the best-fit value of q. To get more information on the parameters, we use the Markov chain Monte Carlo (MCMC) sampling algorithm (Lewis & Bridle 2002; Yan et al. 2013). The fitting is performed on three beaming models: (1) a power-law form for $P_\gamma(\gamma)$; (2) a form similar to the relativistic Maxwell-Jüttner distribution for $P_\gamma(\gamma)$; (3) the same form of $P_\gamma(\gamma)$ as model 2, but setting θ_1 and θ_2 as free parameters. The fit values are summarized in Table 5. The posterior probability distributions and two-dimensional (2D) confidence contours of parameters in our beaming models are given in Figure 7. With the 2D contours, one can inspect the degeneracies between the input parameters (e.g., Yan et al. 2016).

Figure 8 shows how the best-fit beaming models reproduce the core RLF of SSRQs. It seems that all the three models are applicable. Model 2 has fewer free parameters than Model 1. Having the same number of free parameters as Model 1, Model 3 has the advantage of constraining the range of viewing angles. It gives values of $\theta_1 = 44.8^{+6.6}_{-6.7}$ degrees and $\theta_2 = 8.0^{+1.6}_{-0.4}$ degrees. The value of θ_2 is slightly smaller than that of 14° given by Padovani & Urry (1992). According to the unification scheme of AGNs, θ_1 marks the division between RGs and SSRQs, and θ_2 is the demarcation angle between FSRQs and SSRQs. From the relative numbers between RGs and quasars, Barthel (1989) concluded that $\theta_1 = 44.^\circ4$, very close to our result. Based on the monitoring observations with the Very Long Baseline Array (VLBA), Savolainen et al. (2010) reported that 44 of 45 FSRQs in their sample have viewing angles $\leqslant 8.^\circ5$, and only one has a viewing angle of $14.^\circ8$. Their statistics are in good agreement with the results of our analysis.

Table 5
Parameters of the Beaming Models

Parameter	Model 1	Model 2	Model 3
q	$4.679^{+0.003}_{-0.005}$	$4.679^{+0.006}_{-0.017}$	$3.606^{+0.334}_{-0.103}$
k	$-1.38^{+0.10}_{-0.16}$	$3.38^{+0.03}_{-0.04}$	$3.23^{+1.21}_{-0.85}$
γ_1	$3.54^{+0.09}_{-0.10}$	1.01	1.01
γ_2	$34.82^{+12.52}_{-3.95}$	100	100
θ_1	40	40	$44.78^{+6.61}_{-6.65}$
θ_2	14	14	$7.98^{+1.58}_{-0.42}$

Note. Parameters without an error estimate were kept fixed during the fitting stage. The units of θ_1 and θ_2 are degrees.

In Figure 9, we show the distributions of Lorentz factors and Doppler factors predicted by the beaming models. The power-law index of Model 1 is $k = -1.38^{+0.10}_{-0.16}$, which is in agreement with the $k \sim -1.5$ found for the CJ-F survey (Lister & Marscher 1997). Model 1 implies an average Lorentz factor for SSRQs of $\gamma = 11.68^{+1.59}_{-0.70}$. Models 2 and 3 give $\gamma = 10.27^{+0.10}_{-0.13}$ and $\gamma = 9.84^{+3.61}_{-2.50}$, respectively. On average, our result is close to the average Lorentz factor for Fermi-detected FSRQs, which is $\gamma = 11.7^{+3.3}_{-2.2}$ given by Ajello et al. (2012).

6. Discussion

6.1. Comparing Core RLF with Total RLF

Compared with the total RLF, the typical characteristic of the core RLF (see Figure 6) is the negative evolution occurring at a redshift of $z \gtrsim 0.8$. In Figure 10, we plot the core RLF for RGs and the total RLF (also see the "Model A" panel of Figure 3 in Y17) together. Note that for low- and high-luminosity cores, the variation of space density with redshift behaves very similarly, implying a very weak luminosity-dependent evolution. As for the total RLF, however, both the amount of space density changing from redshift zero to the maximum space density, and the peak redshift are strong functions of radio luminosity. Figure 11 shows the variation in the redshift of the peak space density with radio luminosity for the core RLF, compared with that for total RLF. Note for the core RLF, the peak redshift increases very slightly with radio core luminosity, while for the total RLF, the increase is dramatic.

The parametric core RLF in Section 5.2 allows us to determine the DE and LE for radio cores. They are given by Equations (16) and (17). In the upper panel of Figure 12, we plot the LE function of radio cores compared with that of the total source. Both the cores and total source show a positive LE, but the LE of the cores is less dramatic. The positive LE suggests that both the radio cores and lobes at higher redshift are systematically brighter than those of today. A possible explanation is that both the average density of the universe and the gas fraction are higher (Best et al. 2014) at higher redshifts, so that the radio lobes of AGNs remain more confined and adiabatic expansion losses are lower, leading to higher synchrotron luminosities (e.g., Barthel & Arnaud 1996). On the other hand, the positive LE for cores is milder than that for lobes, implying that the denser environment at high redshift has relatively less impact on the core luminosity. Less interaction

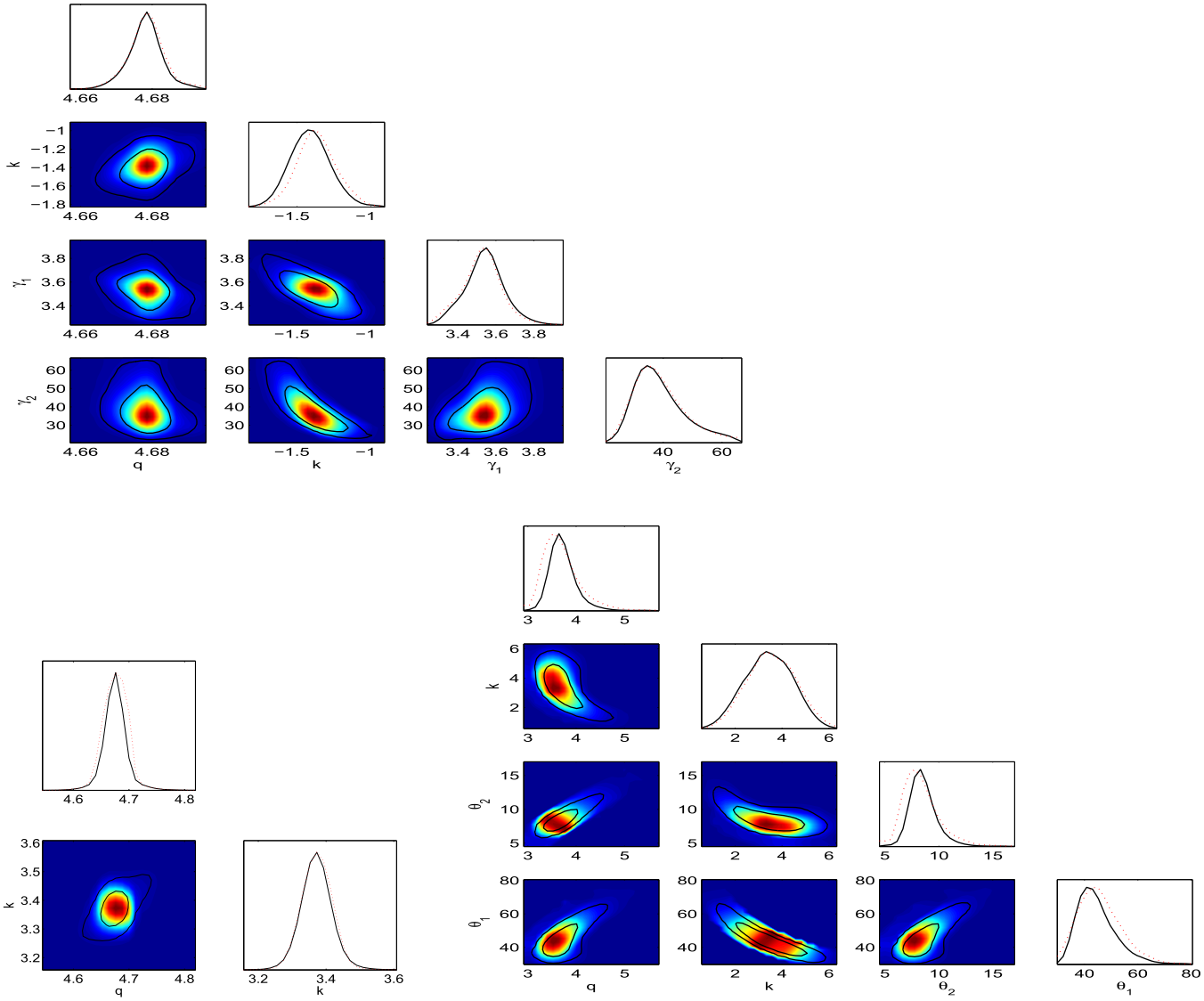

Figure 7. Posterior probability distributions and 2D confidence contours of parameters in the beaming models. The red dash-dotted curves are the mean likelihoods of MCMC samples and the black solid curves are the marginalized probabilities. The contours are for 1σ and 2σ levels. The upper, lower left, and lower right panels correspond to models 1, 2, and 3 respectively.

with external environment often means less shocks, less energy dissipation, and less radio emission (Falcke et al. 2004).

The DE function of the cores cannot be compared directly with that of the total source. We define the normalized DE function as:

$$\varrho(z) = \int_{L_{\rm min}}^{L_{\rm max}} \rho(z, L)dL \Big/ \int_{L_{\rm min}}^{L_{\rm max}} \rho(z=0, L)dL. \quad (31)$$

The normalized DE functions of radio core and total source are shown in the lower panel of Figure 12. The two functions are in good agreement within the uncertainty range, indicating that the core and lobes co-evolve with redshift. It is possible that they are not completely consistent, e.g., episodic AGN activity could cause deviations. This would allow the presence of RGs with a "switched-off core (e.g., Marecki & Szablewski 2009), or having dying radio lobes from an earlier active epoch along with newly restarting jets and cores (e.g., Murgia et al. 2011). But such sources do not appear to dominate our sample.

Falcke et al. (1995) argued that the difference between radio-loud and radio-weak is established already on the parsec scale. We find that the DE function of radio cores peaks at $z \sim 0.8$ and then rapidly decreases, indicating that core-bright radio-loud AGNs at high redshift are less numerous. The redshift at which radio cores peak is lower than the redshift of BH growth. The reason for this is not entirely clear but it is presumably related to redshift-dependent accretion efficiency and jet triggering. For example, simulations of AGN evolution by Hirschmann et al. (2014) have revealed that the number of BHs accreting close to the Eddington rate decrease with increasing redshift. This implies that the dominant mechanism of AGN fueling changes with cosmic time from cold gas accretion via major mergers to radiatively inefficient accretion directly from hot gas halos (Rigby et al. 2015).

In the lower panel of Figure 12, we also plot the normalized DE of Fermi-detected FSRQs as a function of redshift (adopted from the Figure 15 of Ajello et al. 2012). The general trend of their result is consistent with our determination. Nevertheless, it

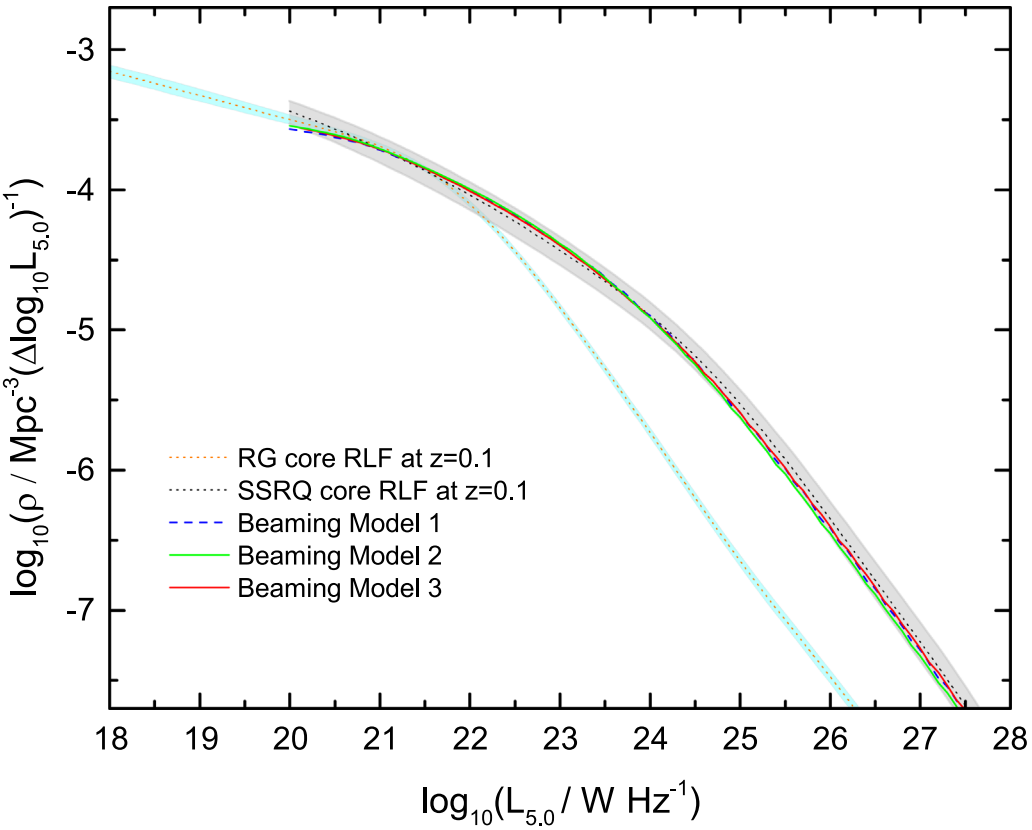

Figure 8. Core RLFs of RGs (orange dotted line) and SSRQs (black dotted line) at $z = 0.1$ and the best-fit beaming models described in Section 5.3. The light shaded areas represent the uncertainties due to the incompleteness of spectral indices.

seems that both the decline in the space density after the redshift peak and the increase in space density leading up to the redshift peak are more dramatic than that of our result. Also note that their peak redshift is $z \sim 0.6$, which is smaller than our determination of $z \sim 0.8$. We speculate that the above difference is caused because the Fermi-detected FSRQ sample bias to those extreme FSRQs with, on average, faster apparent jet speeds and smaller viewing angles (e.g., Lister et al. 2009; Savolainen et al. 2010). It represents an extreme sub-sample of FSRQs.

6.2. Other Input Models of Total RLF

Our key equation for determining the core RLF is given by Equation (20). Given $p(\log L_c|\log L_t)$, the calculation of core RLF depends on the model adopted for the total RLF. In order to rule out the possibility that a different total RLF model may significantly change the main result, we need to perform a comparison test. In the test, we adopt the Model C of Y17 as the new total RLF, for which $\rho_t(z, L_t)$ and $e_1(z)$ are also given by Equation (15) and (16), while $e_2(z)$ is given by

$$e_2(z) = 10^{k_1 z^2 + k_2 z}. \quad (32)$$

Model C permits the possibility of negative LE at high redshift, and it was comparable to Model A in fitting the data of Y17. Figure 13 compares the core RLFs derived for the two total RLF models. The black, cyan, red, blue and green dashed lines show the core RLFs at $\log_{10} L_{5.0\,\mathrm{GHz}} = 19$, 21, 23, 25, and 27, respectively, for Model C. The solid curves represent the core RLF for RGs determined in Section 5.1. The core RLFs are not significantly different at $z \lesssim 3$. Their only difference lies in the steepness of the high-redshift decline of ρ_c. Due to a lack of high-redshift samples, the total RLFs in Y17 cannot conclude whether the high-redshift decline of ρ_t is sharp or shallow. The core RLFs here inherit such uncertainty.

6.3. Luminosity-dependent Evolution

In the past decades, it has been established that the evolution of the LFs of AGNs is luminosity-dependent (e.g., Waddington et al. 2001; Ueda et al. 2003; Hasinger et al. 2005; Hopkins et al. 2007; Croom et al. 2009; Aird et al. 2010; Rigby et al. 2011; Ajello et al. 2012; Zeng et al. 2013; Delvecchio et al. 2014). Physically, this was usually interpreted as a sign of cosmic downsizing, where the most massive black holes form at earlier epochs than their less massive counterparts (Rigby et al. 2015). To describe the luminosity-dependent evolution of optical, X-ray, and γ-ray LFs, the luminosity-dependent density evolution (LDDE) model was developed and became popular. But the LDDE model is unable to model the steep-spectrum RLF (Y17). We thus develop a mixture evolution scenario (Yuan et al. 2016, Y17), which suggests that the evolution of RLF is due to a combination of DE and LE. In essence, the DE determines when the density curve will peak and when it will decline, while the LE can shift the location of peaks according to different luminosities, such that a luminosity-dependent evolution is a natural result. The mixture evolution scenario is especially suitable for interpretation of the difference between core and total RLFs: although the cores and lobes experience

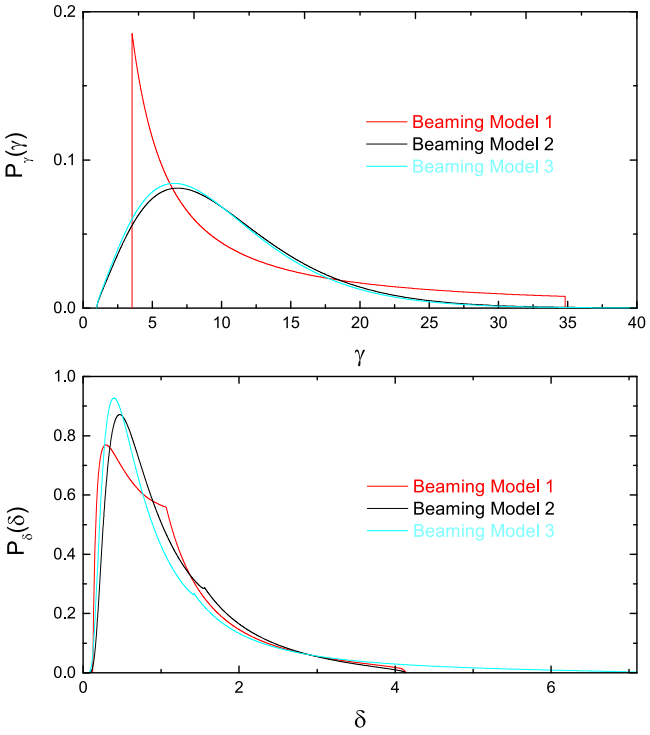

Figure 9. Distributions of Lorentz factors (upper panel) and Doppler factors (lower panel) predicted by the beaming models.

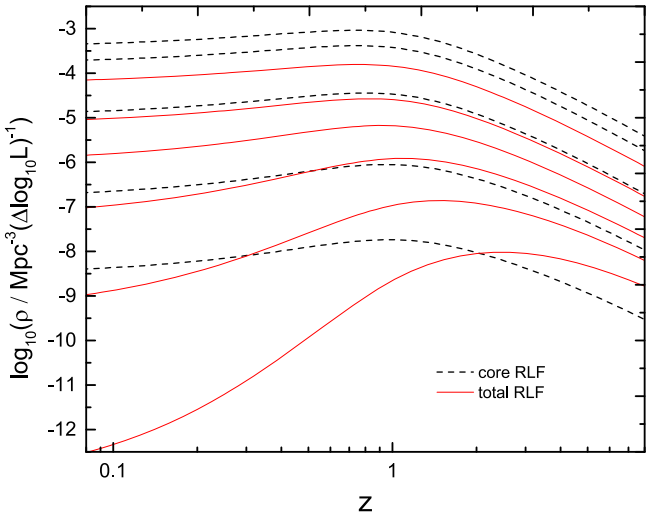

Figure 10. Comparison between core RLF for RGs and total RLF (Model A of Y17). From top to bottom, the black dashed lines show the core RLFs at $\log_{10}L_{5.0\,\mathrm{GHz}} = 19$, 21, 23, 25, and 27, respectively, and the red solid lines represent the total RLFs at $\log_{10}L_{408\,\mathrm{MHz}} = 23.0$, 24.5, 25.5, 26.5, 27.5, and 28.5 respectively.

synchronous DE, the cores have significantly weaker LE than lobes.

6.4. Comparison with Previous Studies

In the decades since the discovery of radio AGNs, studies on the core RLF have been few. An early determination of the core RLF was given by Falcke et al. (2004). Based on the 150 mas-scale radio nuclei in the Palomar sample, they derived the 15 GHz core RLF of nearby galaxies (mainly consisting of low-luminosity AGNs). This result is shown as black open circles with error bars in Figure 14. Note that Falcke et al.'s (2004) errors are large and within those errors his core RLF is in reasonable agreement with our result. Nevertheless, at the faint end ($\log_{10}L_{5.0\,\mathrm{GHz}} < 21$) his core RLF appears to be higher than our RG core RLF. This is because at the faint end our core RLF may not sufficiently consider the contribution of low-luminosity AGNs.

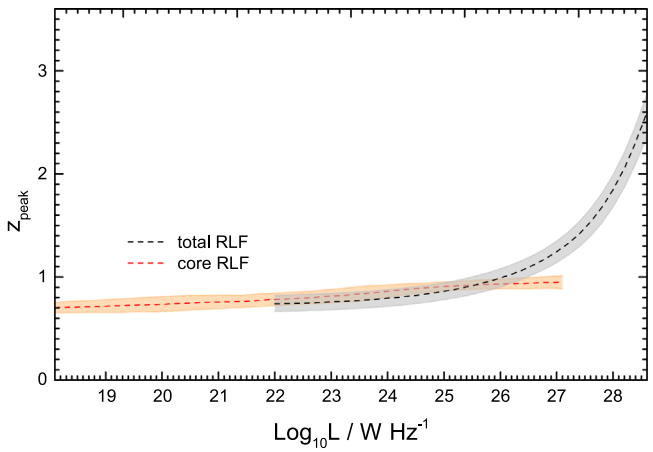

Figure 11. Variation in the redshift of the peak space density with radio luminosity for the core RLF, compared with that for total RLF.

Based on a combined sample of steep-spectrum radio AGNs, Yuan & Wang (2012) investigated the core RLF using the binned $1/V_{\mathrm{max}}$ method. However, that core sample was not strictly a flux-limited complete sample, and the minimum core flux density of the sample was used as the flux limit to estimate $1/V^i_{\mathrm{max}}$. This would significantly underestimate the core RLF (Yuan & Wang 2013). Thus, the result in that work can only be regarded as a rough estimation. Yuan & Wang (2012) concluded that the comoving number density of radio cores displays a persistent decline with redshift, implying a strong negative evolution. Now it seems that this conclusion partly reflects the truth. The result based on the more rigorous method in this work indicates that the negative evolution of cores occurs at a redshift of $z \gtrsim 0.8$.

Using a sample of 202 radio sources from the Australia Telescope 20 GHz (AT20G) survey identified with galaxies from the 6dF Galaxy Survey (6dFGS), Sadler et al. (2014) made the first measurement of the local RLF of RGs at 20 GHz. Since the radio emission from active galaxies at 20 GHz arises mainly from the galaxy core, rather than from extended radio lobes (e.g., Sadler et al. 2006), the measurement of Sadler et al. (2014) can be treated as the local core RLF. In Figure 14, their result is shown as red solid squares, and is in good agreement with our core RLF.

Another study involving the core RLF was performed by Di Mauro et al. (2014, hereafter D14). They obtained the core RLF from the total RLF of Willott et al. (2001) by a simple transformation:

$$\rho_c(z, L_c) = \rho_t(z, L_t(L_c))\frac{d\log L_t}{d\log L_c}, \quad (33)$$

where $L_t(L_c)$ and $d\log L_t/d\log L_c$ derive from the total–core correlation, i.e.,

$$\log L_c^{5\,\mathrm{GHz}} = (4.2 \pm 2.1) + \log L_t^{1.4\,\mathrm{GHz}}(0.77 \pm 0.08). \quad (34)$$

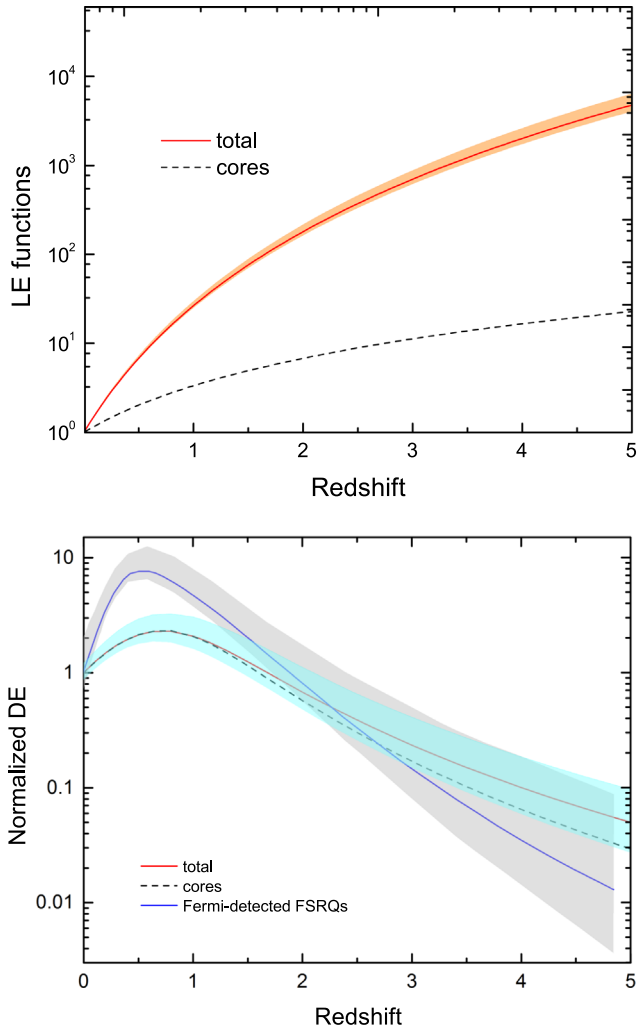

Figure 12. LE (upper panel) and normalized DE (lower panel) as functions of redshift. The red solid and black dashed lines represent the total and cores, respectively. In the lower panel also plotted is the normalized DE of Fermi-detected FSRQs (blue solid line) as a function of redshift (derived from the Figure 15 of Ajello et al. 2012). The light shaded areas take into account the 1σ error bands.

The premise of using Equation (33) is that L_c is a function of L_t. But obviously, there is no definite functional relationship between L_c and L_t. The only rigorous concept describing the correlation between L_c and L_t is conditional probability, which can be well measured via the copula method, while the linear fit like Equation (34) is only a rough sketch. Thus, the estimation obtained with Equations (33) and (34) may distort the true core RLF. In Figure 14, we show the core RLF derived by D14 as a red solid line.

6.5. The Copula versus the Non-copula Method

Both the copula approach here and D14's simpler approach are indirect techniques of estimating the core RLF. The precision significantly depends on how accurately the $L_C - L_T$ correlation is measured. Unlike our copula method, D14's approach does not incorporate the intrinsic dispersion in the $L_C - L_T$ correlation. To further compare the core RLF derived by copula with that using a non-copula approach, we derive the core RLF by applying D14's transformation approach to our total RLF (Y17 model A). This is shown as the green dashed line in Figure 14. Note that D14s core

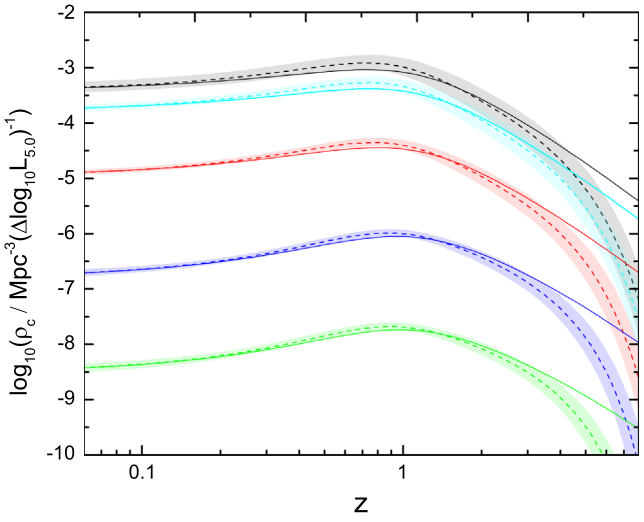

Figure 13. Core RLF for RGs determined based on a different total RLF model (the Model C of Y17). The black, cyan, red, blue, and green dashed lines show the core RLFs at $\log_{10} L_{5.0\,\mathrm{GHz}} = 19$, 21, 23, 25, and 27, respectively. The light shaded areas take into account the uncertainties due to the incompleteness of spectral indices, as well as the 1σ error propagated from the Model C total RLF by Y17. The solid curves represent the core RLF for RGs determined in Section 5.1.

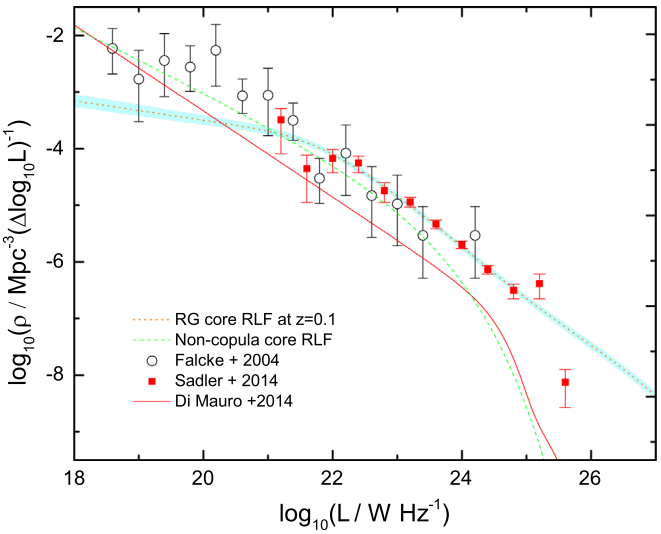

Figure 14. Comparison of our core RLFs with previous results. The orange dotted line shows our RG core RLF at $z = 0.1$, with the cyan band taking into account the combined uncertainty due to the incompleteness of spectral indices, as well as the 1σ error propagated from the total RLF by Y17. The green dashed line shows the core RLF derived by non-copula method. The black open circles with error bars represent the 15 GHz core RLF of nearby galaxies measured by Falcke et al. (2004). The local RLF of RGs at 20 GHz measured by Sadler et al. (2014) is shown as red solid squares. The red solid line shows the core RLF derived by Di Mauro et al. (2014). A flat spectrum for the core ($\alpha_c = 0$) is assumed, ensuring that core RLFs at different frequencies can be compared directly.

RLF and our non-copula core RLF agree, but they are significantly different from the core RLF derived using the copula method. They are steeper at both faint ($\log_{10} L_{5.0\,\mathrm{GHz}} < 21$) and bright ($\log_{10} L_{5.0\,\mathrm{GHz}} > 24$) luminosities. In general, they are inferior to the copula-based result in fitting the observed data, particularly those data obtained more recently.

7. Summary and Conclusions

The main results of this work are as follows.

1. We verified, through a partial correlation analysis, that the correlation between the core and total radio luminosities of radio AGNs is significant. We then explored the correlation via a powerful statistical tool called "Copula." For both RGs and SSRQs, we find that the number 13 Archimedean copula of Nelson (2006) can well describe the $L_c - L_t$ correlation. Our results find the copula is tail-independent, implying that when the cores reach extreme luminosities, the probability that lobes also show extreme luminosities tends to zero.
2. The conditional probability distribution $p(\log L_c|\log L_t)$ is obtained based on the copula-described $L_c - L_t$ relation. We then derive the core RLFs as a convolution of $p(\log L_c|\log L_t)$ and the total RLF that was determined by Yuan et al. (2017). The core RLFs are derived separately for RGs and SSRQs according to their own copula description. Our results are in reasonable agreement with studies that have used radio emission at high frequency as a measure of the core emission.
3. We argue that for a specific population of AGNs (e.g., SSRQs), the jet angles should be (randomly) distributed within $\theta_2 \leqslant \theta \leqslant \theta_1$ but not necessarily $0^\circ \leqslant \theta \leqslant 90^\circ$. Thus, the formula calculating the PDF $P_\delta(\delta)$ for δ by Lister (2003) should be modified to apply to more general conditions. In this work we give the generalized formula for deriving $P_\delta(\delta)$.
4. By assuming that the RG core RLF is the intrinsic core RLF, we find the SSRQ core RLF can be reproduced by imposing a Doppler beaming effect on the RG core RLF. Consistent with previous studies, we find that the distribution of Lorentz factor can be described by a power-law form, and a form similar to the relativistic Maxwell-Jüttner distribution is also applicable. Our preferred beaming model suggests that SSRQs have an average Lorentz factor of $\gamma = 9.84^{+3.61}_{-2.50}$, and that most are seen within $8^\circ \lesssim \theta \lesssim 45^\circ$ of the jet axis.
5. We find that while the DE of the core and total RLFs match within uncertainties, there is a significant difference in their luminosity evolution. The core RLF presents a very weak luminosity-dependent evolution, with the number density peaking around $z\sim 0.8$ for all luminosities. The redshift at which core RLF peaks is lower than that of the peak of BH growth. The reason for this is not entirely clear, but it is presumably related to redshift-dependent accretion efficiency and jet triggering.

We are grateful to the referee for useful comments that improved this paper. We acknowledge the financial support from the National Natural Science Foundation of China through grants No. 11603066, 11573060, 11661161010, and U1738124. We thank Xiaolin Yang, Ming Zhou, Guobao Zhang, and Dahai Yan for useful discussions. B.Z. is supported by the National Thousand Young Talents program of China. J.M. is supported by the National Natural Science Foundation of China 11673062, the Hundred Talent Program, the Major Program of the Chinese Academy of Sciences (KJZD-EW-M06), and the Overseas Talent Program of Yunnan Province. The authors gratefully acknowledge the computing time granted by the Yunnan Observatories, and provided on the facilities at the Yunnan Observatories Supercomputing Platform. This research has made use of the NASA/IPAC Extragalactic Database (NED), which is operated by the Jet Propulsion Laboratory, California Institute of Technology, under contract with the National Aeronautics and Space Administration.

Appendix A
The Sample of 503 Sources

Table 6 contains the 503 sources of Sample II.

Table 6
Summary of Sample

IAU	Other Name	z	$S_{t0.408}$ Jy	α_t	$S_{\rm core5.0}$ mJy	α_c	Classification	References
0101−649	⋯	0.1630	1.15	0.55	179.2	−0.22	G	1
0736+017	⋯	0.1910	2.840	0.21	1780	⋯	Q	2
2315−425	PMN J2317−4213	0.0560	0.97[i]	0.80	<20.6	0.49	G	1, 37
2316−423	⋯	0.0545	1.67	0.05	139.9	0.1	G	1
0123−016	⋯	0.0180	16.40	0.93	100	−0.3	G	2
0005−199	⋯	0.1223	2.08	0.70	14	−0.54	G	3, 4, 5
0222+36	⋯	0.0327	0.37	0.21	140	−0.47	G	6, 7, 8
1144+352	B2 1144+35B	0.0631	0.33	−0.53	243	⋯	G	7, 18, 25
2308+098	4C09.72	0.432	1.99	0.74	102	⋯	Q	21, 23, 24

Note. Column (1). Source name in IAU designation (B1950). Column (2). Other name if available. Column (3). Spectroscopic redshift. Column (4). Total flux density at 408 MHz in Jy. Those with a flag "i" mean that their $S_{t0.408}$ are interpolated from near frequencies. Column (5). Spectral index near 408 MHz, defined by $S \propto \nu^{-\alpha}$). Column (6). Core flux density at 5 GHz in mJy. Column (7). Core spectral index near 5 GHz. Column (8). Classification: G = radio galaxy; Q = quasar. Column (9). References: (1) Jones et al. (1994), (2) Morganti et al. (1993), (3) Ekers et al. (1989), (4) Slee et al. (1994), (5) Govoni et al. (2000), (6) Hardcastle et al. (2003), (7) Liuzzo et al. (2009), (8) Giroletti et al. (2005), (9) Bridle et al. (1991), (10) Feretti et al. (1984), (11) Fanti et al. (1987), (12) Fanti et al. (1978), (13) Capetti et al. (2002), (14) Capetti et al. (1995), (15) Morganti et al. (1997), (16) Kharb & Shastri (2004), (17) Giovannini et al. (1988), (18) Giovannini et al. (2007), (19) Canosa et al. (1999), (20) Reid et al. (1999), (21) Wright & Otrupcek (1990), (22) Large et al. (1981), (23) Large et al. (1991), (24) Nilsson (1998), (25) Colla et al. (1970), (26) Douglas et al. (1996), (27) Ficarra et al. (1985), (28) Riley (1989), (29) Kellermann et al. (1969), (30) Steenbrugge et al. (2010), (31) Condon et al. (1998), (32) Hales et al. (1990), (33) Lacy et al. (1993), (34) McCarthy et al. (1989), (35) Ekers & Kotanyi (1978), (36) Mantovani et al. (1992), (37) Wright et al. (1994), (38) White & Becker (1992).

(This table is available in its entirety in machine-readable form.)

Appendix B
Partial Correlation Analysis

In statistics, partial correlation measures the degree of association between two random variables, after eliminating the effect of all other random variables. Suppose there are three random variables x_i, x_j, and x_k. The correlation coefficient between two of them, say x_i and x_j, is denoted by r_{ij}. The partial correlation of x_i and x_j given x_k is (Kendall & Stuart 1979)

$$r_{ij|k} = \frac{r_{ij} - r_{ik} r_{jk}}{\sqrt{1 - r_{ik}^2}\sqrt{1 - r_{jk}^2}}. \quad (35)$$

The correlation coefficients r_{ij}, r_{ik}, and r_{jk} can be calculated based on Pearson's, Kendall's, or Spearman's correlation methods. In this work we use the Spearman rank-order correlation coefficient, which is given by Equation (35) of Inoue (2011). According to Kim (2015), the statistics $t_{ij|k}$ of the partial correlation is calculated by

$$t_{ij|k} = r_{ij|k}\sqrt{\frac{N - 2 - g}{1 - r_{ij|k}^2}}, \quad (36)$$

where N is the sample size and g is the total number of given variables (here $g = 1$). The probability of the null hypothesis that x_i and x_j are uncorrelated, i.e., the p-value, is given by

$$p_{ij|k} = 2\Phi_t(-|t_{ij|k}|, N - 2 - g), \quad (37)$$

where $\Phi_t(\cdot)$ is the cumulative density function of a Student's t distribution with the degree of freedom $N - 2 - g$ (see Kim 2015, for details).

Appendix C
Doppler Factor Distributions

We determine the PDF $P_\delta(\delta)$ that describes the expected distributions of Doppler factors for a randomly oriented, two-sided jet population. Suppose the PDF of Lorentz factors is $P_\gamma(\gamma)$ which is valid for $\gamma_1 \leqslant \gamma \leqslant \gamma_2$. As mentioned in Section 5.3, SSRQs have their radio axes within $\theta_1 \gtrsim \theta \gtrsim \theta_2$, and $\theta_1 = 40°$, $\theta_2 = 14°$. Thus, the viewing angles are distributed according to

$$P_\theta(\theta) = \frac{\sin\theta}{\cos\theta_2 - \cos\theta_1}. \quad (38)$$

We define

$$f_\delta(\gamma, \theta) = (\gamma - \sqrt{\gamma^2 - 1}\cos\theta)^{-1}, \quad (39)$$

and

$$g_\pm(\delta, \theta) = \frac{1 \pm \cos\theta\sqrt{1 - \delta^2\sin^2\theta}}{\delta\sin^2\theta}. \quad (40)$$

Given $\theta_2 \leqslant \theta \leqslant \theta_1$ and $\gamma_1 \leqslant \gamma \leqslant \gamma_2$, the possible Doppler factors range from

$$\delta_{\min} = f_\delta(\gamma_2, \theta_1) \quad (41)$$

to

$$\delta_{\max} = \begin{cases} f_\delta(\gamma_1, \theta_2), & \frac{1}{\sin\theta_2} < \gamma_1 \\ f_\delta(\gamma_2, \theta_2), & \frac{1}{\sin\theta_2} > \gamma_2 \\ \frac{1}{\sin\theta_2}, & \gamma_1 \leqslant \frac{1}{\sin\theta_2} \leqslant \gamma_2. \end{cases} \quad (42)$$

According to the theory of probability transformation for several variables (e.g., Lister 2003), the PDF for δ is given by

$$P_\delta(\delta) = \begin{cases} \frac{\delta^{-2}}{\cos\theta_2 - \cos\theta_1}\int_{A(\delta)}^{B(\delta)} \frac{P_\gamma(\gamma)}{\sqrt{\gamma^2 - 1}} d\gamma, & \delta_{\min} \leqslant \delta \leqslant \delta_{\max}, \\ 0, & \text{elsewhere}, \end{cases} \quad (43)$$

where the upper limit of integral is

$$B(\delta) = \min[\gamma_2, g_+(\delta, \theta_2)]. \quad (44)$$

The lower limit of the integral is a bit more complex than that discussed by Lister (2003, see their Equation (23)). It depends on the relationship between γ_1, γ_2, θ_1, and θ_2.

1. If $\frac{1}{\sin\theta_1} < \frac{1}{\sin\theta_2} < \gamma_1 < \gamma_2$, then

$$A(\delta) = \begin{cases} g_+(\delta, \theta_1), & \delta_{\min} \leqslant \delta < f_\delta(\gamma_1, \theta_1) \\ \gamma_1, & f_\delta(\gamma_1, \theta_1) \leqslant \delta \leqslant f_\delta(\gamma_1, \theta_2). \end{cases} \quad (45)$$

2. If $\frac{1}{\sin\theta_1} < \gamma_1 < \frac{1}{\sin\theta_2} < \gamma_2$, then

$$A(\delta) = \begin{cases} g_+(\delta, \theta_1), & \delta_{\min} \leqslant \delta < f_\delta(\gamma_1, \theta_1) \\ \gamma_1, & f_\delta(\gamma_1, \theta_1) \leqslant \delta < f_\delta(\gamma_1, \theta_2) \\ g_-(\delta, \theta_2), & f_\delta(\gamma_1, \theta_2) \leqslant \delta \leqslant \frac{1}{\sin\theta_2}. \end{cases} \quad (46)$$

3. If $\frac{1}{\sin\theta_1} < \gamma_1 < \gamma_2 < \frac{1}{\sin\theta_2}$, then

$$A(\delta) = \begin{cases} g_+(\delta, \theta_1), & \delta_{\min} \leqslant \delta < f_\delta(\gamma_1, \theta_1) \\ \gamma_1, & f_\delta(\gamma_1, \theta_1) \leqslant \delta < f_\delta(\gamma_1, \theta_2) \\ g_-(\delta, \theta_2), & f_\delta(\gamma_1, \theta_2) \leqslant \delta \leqslant f_\delta(\gamma_2, \theta_2). \end{cases} \quad (47)$$

4. If $\gamma_1 < \frac{1}{\sin\theta_1} < \frac{1}{\sin\theta_2} < \gamma_2$, then

$$A(\delta) = \begin{cases} g_+(\delta, \theta_1), & \delta_{\min} \leqslant \delta < f_\delta(\gamma_1, \theta_1) \\ \max[\gamma_1, g_-(\delta, \theta_2)], & f_\delta(\gamma_1, \theta_1) \leqslant \delta < \frac{1}{\sin\theta_1} \\ \max[\gamma_1, g_-(\delta, \theta_2)], & \frac{1}{\sin\theta_1} \leqslant \delta \leqslant \frac{1}{\sin\theta_2}. \end{cases} \quad (48)$$

5. If $\gamma_1 < \frac{1}{\sin\theta_1} < \gamma_2 < \frac{1}{\sin\theta_2}$, then

$$A(\delta) = \begin{cases} g_+(\delta, \theta_1), & \delta_{\min} \leqslant \delta < f_\delta(\gamma_1, \theta_1) \\ \gamma_1, & f_\delta(\gamma_1, \theta_1) \leqslant \delta < \frac{1}{\sin\theta_1}. \\ \max[\gamma_1, g_-(\delta, \theta_2)], & \frac{1}{\sin\theta_1} \leqslant \delta \leqslant f_\delta(\gamma_2, \theta_2) \end{cases} \quad (49)$$

For Equations (48) and (49), what needs to be specifically noted is the situation when $f_\delta(\gamma_1, \theta_1) \leqslant \delta < \frac{1}{\sin\theta_1}$, the integral calculating $P_\delta(\delta)$ is the sum of two parts, i.e., $\int_{A(\delta)}^{A_1(\delta)} + \int_{A_2(\delta)}^{B(\delta)}$, and

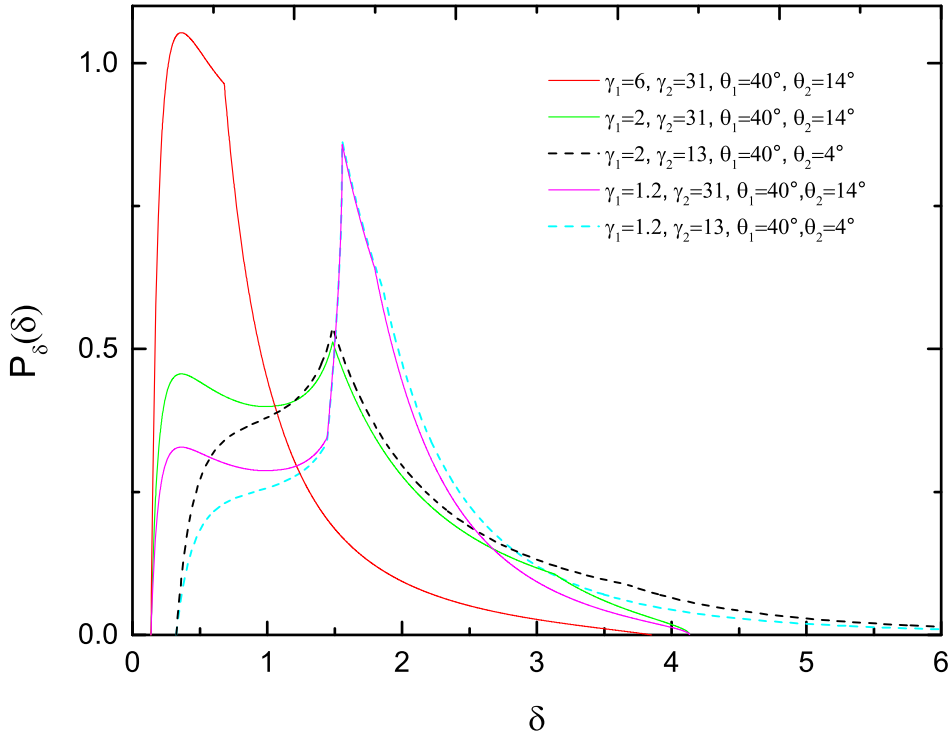

Figure 15. PDF of δ derived from Equation (43) with $P_\gamma(\gamma) \propto \gamma^{-1.5}$. The red, green, black, magenta, and cyan curves show the five cases discussed from Equation (45) to (49), respectively.

$A_1(\delta) = g_-(\delta, \theta_1)$, and $A_2(\delta) = g_+(\delta, \theta_1)$. Figure 15 shows the PDF of δ with $P_\gamma(\gamma) \propto \gamma^{-1.5}$ for the five cases discussed above.

Appendix D
The Conditional Probability Distribution of $\log \mathcal{L}_c$ Given $\log L_c$

From Equation (24), we have

$$\log \mathcal{L}_c = \log L_c + q \log \delta. \tag{50}$$

If q is a constant, according to the univariate theory of probability transformation, the conditional probability distribution of $\log \mathcal{L}_c$ given $\log L_c$ is

$$p(\log \mathcal{L}_c | \log L_c) = \frac{\ln 10}{q} \left(\frac{\mathcal{L}_c}{L_c}\right)^{\frac{1}{q}} P_\delta\left(\left(\frac{\mathcal{L}_c}{L_c}\right)^{\frac{1}{q}}\right). \tag{51}$$

If $q = q_c + \alpha$, where q_c is a constant and α is the spectral index of radio core, q will follow the similar distribution with α. As mentioned in Section 3.2, the distribution of α is well fit by a Gaussian function with mean and sigma given in Table 2. Thus, the PDF for q is

$$P_q(q) = \frac{1}{\sqrt{2\pi}\,\sigma} \exp\left(-\frac{(q-\mu)^2}{2\sigma^2}\right), \tag{52}$$

where $\sigma = 0.397$ and $\mu = q_c + 0.001$. Since $\log \mathcal{L}_c$ is the function of q and δ, the PDF for $\log \mathcal{L}_c$ is

$$p(\log \mathcal{L}_c) = \int P_\delta(\delta) P_q(q) \left| \frac{dq}{d \log \mathcal{L}_c} \right| d\delta. \tag{53}$$

From Equation (50), we have

$$q = \frac{\log \mathcal{L}_c - \log L_c}{\log \delta}, \tag{54}$$

Thus the conditional probability distribution of $\log \mathcal{L}_c$ given $\log L_c$ is

$$p(\log \mathcal{L}_c | \log L_c) = \int_{\delta_{\min}}^{\delta_{\max}} P_\delta(\delta) P_q \times \left(\frac{\log \mathcal{L}_c - \log L_c}{\log \delta}\right) \left| \frac{1}{\log \delta} \right| d\delta. \tag{55}$$

ORCID iDs

Zunli Yuan https://orcid.org/0000-0001-6861-0022
D. M. Worrall https://orcid.org/0000-0002-1516-0336
Jirong Mao https://orcid.org/0000-0002-7077-7195

References

Aird, J., Nandra, K., Laird, E. S., et al. 2010, MNRAS, 401, 2531
Ajello, M., Romani, R. W., Gasparrini, D., et al. 2014, ApJ, 780, 73
Ajello, M., Shaw, M. S., Romani, R. W., et al. 2012, ApJ, 751, 108
Akaike, H. 1974, ITAC, 19, 716
AMI Consortium, Franzen, T. M. O., Davies, M. L., et al. 2011, MNRAS, 415, 2699
Antonucci, R. 1993, ARA&A, 31, 473
Antonucci, R. 2011, arXiv:1101.0837
Avni, Y., & Bahcall, J. N. 1980, ApJ, 235, 694
Baldi, R. D., Capetti, A., & Giovannini, G. 2015, A&A, 576, A38
Baldi, R. D., Williams, D. R. A., McHardy, I. M., et al. 2018, MNRAS, 476, 3478
Barthel, P. D. 1989, ApJ, 336, 606
Barthel, P. D., & Arnaud, K. A. 1996, MNRAS, 283, L45
Benabed, K., Cardoso, J.-F., Prunet, S., & Hivon, E. 2009, MNRAS, 400, 219

Best, P. N., Ker, L. M., Simpson, C., Rigby, E. E., & Sabater, J. 2014, MNRAS, 445, 955
Blandford, R. D., & Königl, A. 1979, ApJ, 232, 34
Botev, Z. I., Grotowski, J. F., & Kroese, D. P. 2010, AnSta, 38, 2916
Bower, R. G., Benson, A. J., Malbon, R., et al. 2006, MNRAS, 370, 645
Bridle, A. H., Baum, S. A., Fomalont, E. B., et al. 1991, A&A, 245, 371
Brocksopp, C., Kaiser, C. R., Schoenmakers, A. P., & de Bruyn, A. G. 2011, MNRAS, 410, 484
Canosa, C. M., Worrall, D. M., Hardcastle, M. J., & Birkinshaw, M. 1999, MNRAS, 310, 30
Capetti, A., Celotti, A., Chiaberge, M., et al. 2002, A&A, 383, 104
Capetti, A., Fanti, R., & Parma, P. 1995, A&A, 300, 643
Cara, M., & Lister, M. L. 2008, ApJ, 674, 111
Chhetri, R., Ekers, R. D., Mahony, E. K., et al. 2012, MNRAS, 422, 2274
Colla, G., Fanti, C., Ficarra, A., et al. 1970, A&AS, 1, 281
Condon, J. J., Cotton, W. D., Greisen, E. W., et al. 1998, AJ, 115, 1693
Croom, S. M., Richards, G. T., Shanks, T., et al. 2009, MNRAS, 399, 1755
Croton, D. J., Springel, V., White, S. D. M., et al. 2006, MNRAS, 365, 11
Delvecchio, I., Gruppioni, C., Pozzi, F., et al. 2014, MNRAS, 439, 2736
Di Mauro, M., Calore, F., Donato, F., Ajello, M., & Latronico, L. 2014, ApJ, 780, 161
Douglas, J. N., Bash, F. N., Bozyan, F. A., Torrence, G. W., & Wolfe, C. 1996, AJ, 111, 1945
Dunlop, J. S., & Peacock, J. A. 1990, MNRAS, 247, 19
Ekers, R. D., & Kotanyi, C. G. 1978, A&A, 67, 47
Ekers, R. D., Wall, J. V., Shaver, P. A., et al. 1989, MNRAS, 236, 737
Fabian, A. C. 2012, ARA&A, 50, 455
Falcke, H., & Biermann, P. L. 1995, A&A, 293, 665
Falcke, H., Körding, E., & Nagar, N. M. 2004, NewAR, 48, 1157
Falcke, H., Malkan, M. A., & Biermann, P. L. 1995, A&A, 298, 375
Fanaroff, B. L., & Riley, J. M. 1974, MNRAS, 167, 31P
Fanti, C., Fanti, R., de Ruiter, H. R., & Parma, P. 1987, A&AS, 69, 57
Fanti, R., Gioia, I., Lari, C., & Ulrich, M. H. 1978, A&AS, 34, 341
Feretti, L., Giovannini, G., Gregorini, L., Parma, P., & Zamorani, G. 1984, A&A, 139, 55
Ficarra, A., Grueff, G., & Tomassetti, G. 1985, A&AS, 59, 255
Ghirlanda, G., Ghisellini, G., Tavecchio, F., Foschini, L., & Bonnoli, G. 2011, MNRAS, 413, 852
Giovannini, G., Cotton, W. D., Feretti, L., Lara, L., & Venturi, T. 2001, ApJ, 552, 508
Giovannini, G., Feretti, L., Gregorini, L., & Parma, P. 1988, A&A, 199, 73
Giovannini, G., Giroletti, M., & Taylor, G. B. 2007, A&A, 474, 409
Giroletti, M., Giovannini, G., & Taylor, G. B. 2005, A&A, 441, 89
Govoni, F., Falomo, R., Fasano, G., & Scarpa, R. 2000, A&A, 353, 507
Hales, S. E. G., Masson, C. R., Warner, P. J., & Baldwin, J. E. 1990, MNRAS, 246, 256
Hardcastle, M. J., Alexander, P., Pooley, G. G., & Riley, J. M. 1998, MNRAS, 296, 445
Hardcastle, M. J., Evans, D. A., & Croston, J. H. 2009, MNRAS, 396, 1929
Hardcastle, M. J., Worrall, D. M., Birkinshaw, M., & Canosa, C. M. 2003, MNRAS, 338, 176
Hasinger, G., Miyaji, T., & Schmidt, M. 2005, A&A, 441, 417
Hirschmann, M., Dolag, K., Saro, A., et al. 2014, MNRAS, 442, 2304
Hopkins, P. F., Richards, G. T., & Hernquist, L. 2007, ApJ, 654, 731
Inoue, Y. 2011, ApJ, 733, 66
Jiang, I.-G., Yeh, L.-C., Chang, Y.-C., & Hung, W.-L. 2009, AJ, 137, 329
Jones, P. A., McAdam, W. B., & Reynolds, J. E. 1994, MNRAS, 268, 602
Kellermann, K. I., Pauliny-Toth, I. I. K., & Williams, P. J. S. 1969, ApJ, 157, 1
Kendall, M., & Stuart, A. 1979, The Advanced Theory of Statistics, Vol. 2 (New York: Oxford Univ. Press)
Kharb, P., & Shastri, P. 2004, A&A, 425, 825
Kim, J., Marrone, D. P., Roy, A. L., et al. 2018, ApJ, 861, 129
Kim, S. 2015, Communications for Statistical Applications and Methods, 22, 665
Koen, C. 2009, MNRAS, 393, 1370
Koen, C., & Bere, A. 2017, MNRAS, 471, 2771
Kroon, J. J., & Becker, P. A. 2016, ApJ, 821, 77
Lacy, M., Rawlings, S., Saunders, R., & Warner, P. J. 1993, MNRAS, 264, 721
Lara, L., Giovannini, G., Cotton, W. D., et al. 2004, A&A, 421, 899
Large, M. I., Cram, L. E., & Burgess, A. M. 1991, Obs, 111, 72
Large, M. I., Mills, B. Y., Little, A. G., Crawford, D. F., & Sutton, J. M. 1981, MNRAS, 194, 693
Lewis, A., & Bridle, S. 2002, PhRvD, 66, 103511
Liao, N.-H., Xin, Y.-L., Fan, X.-L., et al. 2016, ApJS, 226, 17
Lister, M. L. 2003, ApJ, 599, 105
Lister, M. L., Cohen, M. H., Homan, D. C., et al. 2009, AJ, 138, 1874
Lister, M. L., & Marscher, A. P. 1997, ApJ, 476, 572
Liu, F. K., & Zhang, Y. H. 2002, A&A, 381, 757
Liu, Y., & Zhang, S. N. 2007, ApJ, 667, 724
Liuzzo, E., Giovannini, G., Giroletti, M., & Taylor, G. B. 2009, A&A, 505, 509
Mantovani, F., Junor, W., Fanti, R., et al. 1992, MNRAS, 257, 353
Marconi, A., Risaliti, G., Gilli, R., et al. 2004, MNRAS, 351, 169
Marecki, A., & Szablewski, M. 2009, A&A, 506, L33
McAlpine, K., & Jarvis, M. J. 2011, MNRAS, 413, 1054
McAlpine, K., Jarvis, M. J., & Bonfield, D. G. 2013, MNRAS, 436, 1084
McCarthy, P. J., van Breugel, W., & Spinrad, H. 1989, AJ, 97, 36
Merloni, A., & Heinz, S. 2008, MNRAS, 388, 1011
Morganti, R., Killeen, N. E. B., & Tadhunter, C. N. 1993, MNRAS, 263, 1023
Morganti, R., Parma, P., Capetti, A., et al. 1997, A&AS, 126, 335
Mullin, L. M., Riley, J. M., & Hardcastle, M. J. 2008, MNRAS, 390, 595
Murgia, M., Parma, P., Mack, K.-H., et al. 2011, A&A, 526, A148
Murphy, T., Sadler, E. M., Ekers, R. D., et al. 2010, MNRAS, 402, 2403
Nelson, R. B. 1999, An Introduction to Copulas (New York: Springer)
Nelson, R. B. 2006, An Introduction to Copulas (2nd ed.; New York: Springer)
Nilsson, K. 1998, A&AS, 132, 31
Padovani, P. 1992, A&A, 256, 399
Padovani, P., & Urry, C. M. 1992, ApJ, 387, 449
Reid, R. I., Kronberg, P. P., & Perley, R. A. 1999, ApJS, 124, 285
Rigby, E. E., Argyle, J., Best, P. N., Rosario, D., & Röttgering, H. J. A. 2015, A&A, 581, A96
Rigby, E. E., Best, P. N., Brookes, M. H., et al. 2011, MNRAS, 416, 1900
Riley, J. M. 1989, MNRAS, 238, 1055
Sadler, E. M., Ekers, R. D., Mahony, E. K., Mauch, T., & Murphy, T. 2014, MNRAS, 438, 796
Sadler, E. M., Ricci, R., Ekers, R. D., et al. 2006, MNRAS, 371, 898
Sadler, E. M., Slee, O. B., Reynolds, J. E., & Roy, A. L. 1995, MNRAS, 276, 1373
Saikia, D. J., & Jamrozy, M. 2009, BASI, 37, 63
Sato, M., Ichiki, K., & Takeuchi, T. T. 2011, PhRvD, 83, 023501
Savolainen, T., Homan, D. C., Hovatta, T., et al. 2010, A&A, 512, A24
Scherrer, R. J., Berlind, A. A., Mao, Q., & McBride, C. K. 2010, ApJL, 708, L9
Shabala, S. S. 2018, MNRAS, 478, 5074
Slee, O. B., Sadler, E. M., Reynolds, J. E., & Ekers, R. D. 1994, MNRAS, 269, 928
Steenbrugge, K. C., Heywood, I., & Blundell, K. M. 2010, MNRAS, 401, 67
Takeuchi, T. T. 2010, MNRAS, 406, 1830
Ueda, Y., Akiyama, M., Ohta, K., & Miyaji, T. 2003, ApJ, 598, 886
Urry, C. M., & Padovani, P. 1995, PASP, 107, 803
Verdoes Kleijn, G. A., Baum, S. A., de Zeeuw, P. T., & O'Dea, C. P. 2002, AJ, 123, 1334
Waddington, I., Dunlop, J. S., Peacock, J. A., & Windhorst, R. A. 2001, MNRAS, 328, 882
White, R. L., & Becker, R. H. 1992, ApJS, 79, 331
Whittam, I. H., Jarvis, M. J., Green, D. A., Heywood, I., & Riley, J. M. 2017, MNRAS, 471, 908
Whittam, I. H., Riley, J. M., Green, D. A., et al. 2013, MNRAS, 429, 2080
Whittam, I. H., Riley, J. M., Green, D. A., Jarvis, M. J., & Vaccari, M. 2015, MNRAS, 453, 4244
Willott, C. J., Rawlings, S., Blundell, K. M., Lacy, M., & Eales, S. A. 2001, MNRAS, 322, 536
Wright, A., & Otrupcek, R. 1990, PKS Catalog, 0
Wright, A. E., Griffith, M. R., Burke, B. F., & Ekers, R. D. 1994, ApJS, 91, 111
Yan, D., He, J., Liao, J., Zhang, L., & Zhang, S.-N. 2016, MNRAS, 456, 2173
Yan, D., Zhang, L., Yuan, Q., Fan, Z., & Zeng, H. 2013, ApJ, 765, 122
Yates, D. S., Moore, D. S., & Starnes, D. S. 2008, The Practice of Statistics (3rd ed.; San Francisco, CA: Freeman)
Yuan, Z., & Wang, J. 2012, ApJ, 744, 84
Yuan, Z., & Wang, J. 2013, Ap&SS, 345, 305
Yuan, Z., Wang, J., Zhou, M., & Mao, J. 2016, ApJ, 820, 65
Yuan, Z., Wang, J., Zhou, M., Qin, L., & Mao, J. 2017, ApJ, 846, 78
Zeng, H., Yan, D., & Zhang, L. 2013, MNRAS, 431, 997
Zhang, B.-B., Uhm, Z. L., Connaughton, V., Briggs, M. S., & Zhang, B. 2016, ApJ, 816, 72
Zirbel, E. L., & Baum, S. A. 1995, ApJ, 448, 521